Advances in Differential Equations and Control Processes 2026, 33(1), 3821
doi: https://doi.org/10.59400/adecp3821

Article

Adaptive Enriched Rational Spectral Methods with sinh transformations and asymptotic correctors for variable-coefficient singular perturbation problems

Lufeng Yang[1,2]

[1] School of Mathematics and Information Science, North Minzu University, Yinchuan 750021, China; 2003052@nmu.edu.cn

[2] The Collaborative Innovation Center of Scientific Computing and Intelligent Information Processing of Ningxia Province, Yinchuan 750021, China

CITATION

Yang L. Adaptive Enriched Rational Spectral Methods with sinh transformations and asymptotic correctors for variable-coefficient singular perturbation problems. Advances in Differential Equations and Control Processes. 2026; 33(1): 3821. https://doi.org/10.59400/adecp3821

ARTICLE INFO

Received: 12 December 2025
Revised: 20 January 2026
Accepted: 3 February 2026
Available online: 9 February 2026

Abstract: This paper introduces and analyzes novel Enriched Rational Spectral Methods for efficiently solving singular perturbation problems exhibiting sharp boundary layers. While spectral methods are known for their 'spectral accuracy' in solving smooth problems, their performance deteriorates for stiff differential equations because they fail to resolve rapid transitions in the solution. To overcome this limitation, we propose a rational spectral collocation framework enriched with asymptotic corrector functions. These correctors are derived directly from a boundary layer analysis of the variable-coefficient operator itself, enabling them to accurately capture the solution's singular behavior. Two specific schemes are proposed: the Enriched Spectral Method (ESM) and the Enriched Rational Spectral Method combined with a sinh transformation (ERSM-sinh). In ERSM-sinh, the corrector functions are integrated with a sinh transformation whose parameters—layer location and width—are determined from asymptotic estimates. The correction parameters are obtained implicitly by solving the discrete algebraic system arising from the original problem. Extensive numerical experiments on convection-diffusion and reaction-diffusion problems with variable coefficients demonstrate the superior performance of our methods. Results show that ERSM-sinh maintains robust spectral accuracy, significantly outperforms existing approaches such as RSC-SSM and RSCAT for variable-coefficient problems, and achieves high precision with minimal computational cost—even for very small perturbation parameters (e.g., $\varepsilon = 10{-}10$). This work provides a high-resolution, efficient, and generalizable framework for singularly perturbed boundary value problems.

Keywords: Enriched Rational Spectral Method; adaptive sinh transformation; asymptotic corrector function; variable-coefficient singular perturbation problem; boundary layer resolution; convection–diffusion equations; reaction–diffusion equations

1. Introduction

We consider the following singularly perturbed two-point boundary value problem with variable coefficients:

$$\begin{cases} Lu := -\varepsilon u'' + b(x)u' + c(x)u = f(x), \quad x \in \Omega = (x_l, x_r), \\ u(x_l) = u_0, u(x_r) = u_1. \end{cases} \tag{1}$$

where $\varepsilon \ll 1$ is the perturbation parameter, the coefficients satisfy $c(x) \geq \alpha > 0$, $b(x) \geq \beta > 0$, and $f(x)$ are sufficiently smooth. Without loss of generality, the computational domain is initially taken as $(0, 1)$ for simplicity. The method can be

directly applied to any finite interval $[x_l, x_r]$ via a linear coordinate transformation. For small ε, when $b(x) \equiv 0$, the solution typically exhibits sharp boundary layers of width $\mathbb{O}(\sqrt{\varepsilon})$ at $x = 0$ and $x = 1$, posing a significant challenge for numerical approximation. Furthermore, singular perturbation methods have proven to be instrumental across various engineering domains, ranging from the control of complex industrial processes to the robust numerical solution of convection–diffusion–reaction and flow problems [1,2].

Singular perturbation problems—such as fluid mechanics boundary layers, quantum mechanics transition points, and flow at large Reynolds numbers-arise in the mathematical modeling of physical and engineering problems and have attracted considerable research attention in recent decades. Singular perturbation boundary value problems feature either boundary layers or internal layers, where the solution changes drastically. A wide range of theoretical and analytical treatments of these problems can be found in the literature [3–5]. These problems exhibit steep gradients within narrow layers of the domain, leading to rapid changes in the dependent variable. Because of the steep gradients within these layers, standard numerical methods on uniform grids fail to capture the solution accurately without prohibitively fine mesh refinement. Consequently, specialized techniques have been developed, including layer-adapted meshes (Shishkin meshes [6–8]), exponentially fitted schemes [9,10], the Tailored Finite Point Method [11,12], adaptive finite difference methods [13,14], and Non-standard finite difference scheme [15,16]. While these approaches can achieve robust convergence, their accuracy or analysis often depends on a priori knowledge of layer structures and can become complicated for variable-coefficient problems. Commonly used layer-adapted approaches, such as Shishkin and Bakhvalov meshes [14], rely on a priori estimates of the boundary-layer width to construct piecewise-uniform or smoothly-graded grids. While effective, their implementation often requires explicit layer-width information, which may be difficult to obtain for variable-coefficient problems. Coordinate transformations (e.g., the Cosine transform) offer an alternative by clustering points analytically, yet they still typically involve tunable parameters that must be chosen empirically.

Spectral methods are known for their high-order convergence when applied to smooth solutions. To accurately resolve boundary layers, rational spectral collocation approaches combined with coordinate transformations (e.g., sinh transforms) have been developed. These transformations effectively concentrate collocation points within sharp layer regions [17–19]. Recent innovations include the Rational Spectral Collocation-Singularity Separation Method (RSC-SSM) [20], and the Enriched Spectral Method (ESM) with corrector functions [21]. However, a key limitation of RSC-SSM is its reliance on a constant-coefficient subsidiary problem to construct the corrector, which restricts its applicability to genuinely variable-coefficient equations—a fact reflected in the numerical tests in the study of Li et al. [20] being confined to constant coefficients. Other high-accuracy methods, such as the Sinc collocation approach [22] or various physics-informed neural network (PINN)-based approaches, including semi-analytic PINNs, asymptotic PINNs [23–25] have been proposed; however, they either impose stringent analyticity and decay conditions unsuitable for our setting or lack rigorous

error estimates and exhibit sensitivity to small parameters.

While these studies have advanced the field, they still face limitations in addressing singular perturbation problems, particularly those with variable coefficients and complex layer structures. Our work aims to precisely address this limitation by introducing and analyzing two novel spectral approaches: the Enriched Spectral Method (ESM) and the Enriched Rational Spectral Method with a sinh transformation (ERSM-sinh). Both methods incorporate asymptotic corrector functions derived directly from the variable-coefficient operator itself, ensuring consistency and accuracy for general smooth coefficients. In particular, the ERSM-sinh scheme synergistically combines rigorous asymptotic analysis with a sinh-transformed rational spectral collocation framework. It determines layer locations and widths adaptively through asymptotic estimates and embeds this information into the spectral discretization, thereby achieving high-order convergence while handling variable coefficients robustly. Moreover, the stability and long-term behavior of singularly perturbed systems under sustained external influences are of both theoretical and practical importance. The analysis of such systems often relies on establishing uniform a priori estimates and energy-type bounds that are independent of the perturbation parameter. Gol'Dberg [26] established the stability of solutions to a singularly perturbed telegraph system, strengthening the theoretical foundation for analyzing the dynamic behavior of singularly perturbed systems under external forcing.

The superior performance of our proposed schemes, especially ERSM-sinh, is conclusively demonstrated through detailed numerical experiments in Section 4. We test on problems with variable coefficients and compare against existing methods, including RSC-SSM. The results show that our methods maintain spectral accuracy and significantly outperform existing approaches when coefficients are non-constant, confirming their effectiveness in addressing the identified limitations.

The remainder of the paper is structured as follows. Section 2 presents the asymptotic analysis and the sinh transformation underpinning our method. Section 3 details the algorithms for ESM and ERSM-sinh. Section 4 provides comprehensive numerical results validating the theory and demonstrating the methods' efficiency. Finally, conclusions are drawn in Section 5.

2. Preliminaries

Theorem 1. *Let $\Omega = (0,1)$ suppose coefficients $b(x), c(x)$and $f(x)$ are smooth on $\bar{\Omega}$, and there exist constants $\alpha > 0, \beta > 0$ such that $c(x) \geq \alpha > 0,\ b(x) \geq \beta > 0, \forall x \in \bar{\Omega}$. Then for the boundary data $u_0, u_1 \in \mathbb{R}$, the boundary value problem (1) admits a unique solution $u \in C^2(\Omega) \cap C(\bar{\Omega})$ [27]. Moreover, u can be expressed as,*

$$u(x) = z(x) + v(\xi) + \mathbb{O}(\varepsilon), \quad \xi = \frac{1-x}{\varepsilon}, \tag{2}$$

where the smooth component $z(x)$ and the boundary layer component $v(\xi)$ are defined as the solutions to the following reduced problem and boundary problem, respectively:

$$\begin{cases} b(x)z'(x) + c(x)z(x) = f(x), & 0 < x < 1, \\ z(0) = u_0, \end{cases} \tag{3}$$

$$\begin{cases} v''(\xi) + b(1)v'(\xi) = 0, & \xi > 0, \\ v(0) = u_1 - z(1), & \lim\limits_{\xi \to \infty} v(\xi) = 0. \end{cases} \tag{4}$$

We now state a useful lemma, which provides information about the boundary layers occurring in the solution of problem (1).

Lemma 1. *Let us suppose that a function* $u(x)$ *satisfies* $u(0) \geq 0,\ u(1) \geq 0$*, and* $Lu(x) \geq 0,\ \forall x \in \Omega$ *[27]. Then,* $u(x) \geq 0, \forall x \in \bar{\Omega}$.

An immediate consequence of the maximum principle is the following stability result.

Lemma 2. *Let* $u(x)$ *be the solution of (1) [16,25]. Then, the following estimates hold:*

$$|u(x)| \leq M = max(|u_0|, |u_1|) + C\ max\ _{x \in \Omega} |f(x)|, \tag{5}$$

$$|u'(x)| \leq C(1 + \varepsilon^{-1} e^{\frac{\beta}{\varepsilon}(x-1)}). \tag{6}$$

Proof. Let $f_m = max|f(x)|,\ M_0 = max\{|u_0|, |u_1|\}$,and define$y(x) = f_m/\gamma + M_0 - u(x)$,We verify that,

$$\begin{aligned} Ly = -\varepsilon y'' + b(x)y' + c(x)y &= c(x)\left(\tfrac{f_m}{\gamma} + M_0\right) - Lu \\ &= c(x)\left(\tfrac{f_m}{\gamma} + M_0\right) - f(x) \geq 0. \end{aligned}$$

and it is also given that,

$$\begin{cases} y(0) = f_m/\gamma + M_0 - u_0 \geq 0, \\ y(1) = f_m/\gamma + M_0 - u_1 \geq 0. \end{cases}$$

From the Lemma 1, it follows that,

$$y(x) = f_m/\gamma + M_0 - u(x) \geq 0,\ x \in \bar{\Omega}.$$

It implies that,

$$u(x) \leq f_m/\gamma + M_0.$$

Similarly, define $z(x) = u(x) + f_m/\gamma + M_0$, then,

$$Lz = -\varepsilon z'' + b(x)z' + c(x)z = f(x) + c(x)\left(\frac{f_m}{\gamma} + M_0\right) \geq 0,$$

with $z(0) \geq 0$ and $z(1) \geq 0$. By Lemma 1, $w(x) \geq 0$, which implies,

$$u(x) \geq -\left(f_m/\gamma + M_0\right).$$

Combining both bounds yields the expression of (5).

We now derive the derivative estimate. Let $h(x) = f(x) - c(x)u(x)$. Then Equation (4) holds:

$$-\varepsilon u'' + b(x)u' = h(x) \tag{7}$$

Let:

$$\mu(x) = exp\left(-\int_0^x \frac{b(s)}{\varepsilon} ds\right) = exp\left(-\frac{B(x)}{\varepsilon}\right),$$

where $B(x) = \int_0^x b(s)ds$. Multiplying both sides of (7) by $\mu(x)$ yields:

$$(\mu(x)u^{'}(x))^{'} = \frac{h(x)}{\varepsilon}\mu(x).$$

Integrate form 0 to x and rearrange to get:

$$\mu(x)u^{'}(x) = \mu(0)u^{'}(0) + \frac{1}{\varepsilon}\int_0^x h(s)\mu(s)ds.$$

Then we have:

$$u^{'}(x) = u^{'}(0)exp\left(\frac{B(x)}{\varepsilon}\right) + \frac{1}{\varepsilon}\int_0^x h(s)exp\left(\frac{B(x) - B(s)}{\varepsilon}\right) ds. \tag{8}$$

From estimate (5), we obtain,

$$|h(x)| \leq |f(x)| + |c(x)|M \leq C(\|f\|_{L_\infty} + M).$$

Additionally, based on the boundary conditions $u(0) = u_0$ and $u(1) = u_1$, it can be deduced that,

$$u(1) = u(0) + \int_0^1 u^{'}(x)dx$$

then,we have,

$$\left|\int_0^1 u^{'}(x)dx\right| = |u_1 - u_0| \leq C).$$

Since $u'(x)$ is continuous on [1], it follows that the initial derivative is bounded. Specifically, there exists a constant $C > 0$ such that,

$$|u^{'}(0)| \leq C(1 + \varepsilon^{-1}e^{\frac{\beta}{\varepsilon}(x-1)}). \tag{9}$$

Now consider the second term in (8), using the bound $|h(s)| \leq C$ and the inequality,

$$B(x) - B(s) = \int_s^x b(t)dt \geq \beta(x - s) \geq 0,$$

we obtain,

$$\begin{aligned}\left|\frac{1}{\varepsilon}\int_0^x h(s)exp\left(\frac{B(x) - B(s)}{\varepsilon}\right) ds\right| &\leq \frac{C}{\varepsilon}\int_0^x \left(\frac{\beta(x - s)}{\varepsilon}\right) exp \\ &= \frac{C}{\beta}\left[1 - exp\left(-\frac{\beta x}{\varepsilon}\right)\right] \leq \frac{C}{\beta}exp\left(\frac{\beta x}{\varepsilon}\right).\end{aligned}$$

Note that for $x \in [0, 1]$,

$$exp\left(\frac{\beta x}{\varepsilon}\right) = exp\left(\frac{\beta(1 - (1 - x))}{\varepsilon}\right) \leq exp\left(\frac{\beta}{\varepsilon}\right) \cdot exp\left(-\frac{\beta(1 - x)}{\varepsilon}\right)$$

Therefore, the bound for the second term in (8) becomes,

$$\left|\frac{1}{\varepsilon}\int_0^x h(s)exp\left(\frac{B(x)-B(s)}{\varepsilon}\right)ds\right| \leq C\varepsilon^{-1}exp\left(-\frac{\beta(1-x)}{\varepsilon}\right) \tag{10}$$

Combining (8), (9) and (10), we obtain the derivative estimate,

$$|u^{'}(x)| \leq C(1+\varepsilon^{-1}e^{\frac{\beta}{\varepsilon}(x-1)}).\square$$

2.1. Asymptotic expansion approximation

The construction of the Rational Spectral Method (RSM) requires using the problem's exact solution to analyze the position and width of the boundary layer. Two relevant theorems and their proofs have been provided in the study of Li et al. [20]; in this paper, only their conclusions are presented to enable their application in subsequent sections.

Lemma 3. *If $b(x) > 0$, the solution of (1) has the following asymptotic expansion [27],*

$$u(x) = z(x) + \bar{v}(\xi) + \mathbb{O}(\varepsilon),$$

where,

$$\bar{v}(\xi) = \begin{cases} v(\xi), & 0 \leq \xi \leq T, \\ 0, & \xi > T, \end{cases} \qquad T = -\frac{1}{\beta}\ln\frac{\varepsilon}{|\beta - w(1)|},$$

and the smooth component z(x) is the solution of (3), and $v(x)$ is the solution of (4).

Lemma 3 indicates that the boundary layer for the convection-diffusion problem is located at the right endpoint $x = 1$, with a width of $\mathbb{O}(\mu)$, where $\mu = T\varepsilon$.

Lemma 4. *If $b(x) \equiv 0$, the solution of (1) has the following asymptotic expansion [24]:*

$$u(x) = z(x) + \bar{v}(x) + \mathbb{O}(\sqrt{\varepsilon}),$$

where,

$$\bar{v}(x) = \begin{cases} v(x), & x \in [0, \tau_0] \cup [1-\tau_0, 1], \\ 0, & x \in [\tau_0, 1-\tau_0], \end{cases} \qquad 0 < \tau_0 = -\frac{\sqrt{\varepsilon}}{\alpha}\ln\sqrt{\varepsilon} \ll 1,$$

and the smooth component $z(x)$ is the solution of (3), and the lay component $v(x)$ satisfies,

$$\begin{cases} c(x)v(x) = 0, & \forall x \in (0,1), \\ v(0) = u_0 - z(0), & v(1) = u_1 - z(1). \end{cases}$$

Lemma 4 shows that the solution $u(x)$ to the reaction-diffusion problem exhibits twin boundary layers in the regions $[0, \tau_0]$ and $[1-\tau_0, 1]$ each with a width of $\mathbb{O}(\mu)$, where $\mu = \tau_0$.

2.2. Rational spectral collocation method in barycentric form

A rational function $p_N(x)$ in barycentric form approximating $u(x)$ can be expressed as [27]:

$$u(x) \approx p_N(x) = \frac{\sum_{k=0}^{N}\frac{\omega_k}{x-x_k}u(x_k)}{\sum_{k=0}^{N}\frac{\omega_k}{x-x_k}}, \tag{11}$$

where $\{x_k\}_{k=0}^N$ are distinct interpolation points and the barycentric weights $\{\omega_k\}_{k=0}^N$ can be calculated using the formula:

$$\omega_k = \frac{1}{\prod_{j=0, j\neq k}^{N}(x_k - x_j)}. \tag{12}$$

In practical applications, the Chebyshev-Gauss-Lobatto points $x_k = -cos(k\pi/N)$ for $k = 0, 1, \cdots, N$, are commonly used. For these points, the corresponding barycentric weights are given in the study of Bansal et al. [28].

$$\omega_0 = \frac{1}{2}, \omega_k = (-1)^k, k = 1, 2, \cdots, N-1, \omega_N = \frac{(-1)^N}{2}. \tag{13}$$

The convergence analysis of the rational interpolation polynomial in barycentric form with transformed Chebyshev points is as follows.

Theorem 2. *Let D_1, D_2 be two domains of $\mathbb{C}$ containing $J = [-1, 1]$ and a real interval I, respectively [28]. Let $g : D_1 \to D_2$ be a conformal map with $g(J) = I$ and let $f : D_2 \to \mathbb{C}$ be such that the composition $f \circ g : D_1 \to \mathbb{C}$ is analytic inside and on an ellipse $E_\rho (\subset D_1)$ (with $foci \pm 1$ and the sum of its major and minor axes equal to $\rho > 1$). Let $p_N(x)$ be the rational interpolant of u at the transformed Chebyshev points $\widehat{x}_k := g(-cos(k\pi/N))$. Then, $\forall x \in [-1, 1]$,*

$$\|p_N(x) - u(x)\| = \mathbb{O}(\rho^{-N}). \tag{14}$$

The key advantage of representing a rational interpolant in barycentric form is that its derivatives can be computed efficiently using differentiation matrices, avoiding the repeated application of the quotient rule. The *p*-th derivative of p_N at the point x_j can be expressed as,

$$p_N^{(n)}(x_j) = \sum_{k=0}^{N} \frac{d^n}{dx^n} \left(\frac{\frac{\omega_k}{x-x_k} u(x_k)}{\sum_{l=0}^{N} \frac{\omega_l}{x-x_l}} \right)_{x=x_j} = \sum_{k=0}^{N} D_{jk}^{(n)} u(x_k), \quad j = 0, 1, \cdots, N. \tag{15}$$

Let $D^{(1)}$ denotes the first-order differentiation matrix and $D^{(2)}$ denotes the second-order differentiation matrix, which are used to compute derivatives of rational interpolants in barycentric form. The entries of these matrices are given in the study of Tee and Trefethen [29].

$$D_{jk}^{(1)} = \begin{cases} \frac{\omega_k}{\omega_j (x_j - x_k)}, & j \neq k, \\ -\sum_{i\neq k} D_{ji}^{(1)}, & j = k, \end{cases} \quad D_{jk}^{(2)} = \begin{cases} 2D_{jk}^{(1)} \left(D_{jj}^{(1)} - \frac{1}{x_j - x_k} \right), & j \neq k, \\ -\sum_{i\neq k} D_{ji}^{(2)}, & j = k. \end{cases} \tag{16}$$

As indicated in Theorem 2, the convergence rate of barycentric-form rational interpolation primarily depends on the region of analyticity u in the complex plane. Therefore, the conformal map g can be chosen to expand the ellipse of analyticity $u \circ g$. This typically yields a better approximation of u than the Chebyshev spectral method with the same number of grid points.

Note that the differentiation matrices (16) depend only on the weights ω_k and the mapped points $\widehat{x}_k$, which eliminates the need to transform the original equation into new coordinates.

2.3. The sinh transform

To approximate functions with a single localized region of rapid variation using barycentric rational interpolation, Tee and Trefethen [29] constructed the conformal map,

$$g_{\lambda,\mu}(x) = \lambda + \mu \sinh\left[\left(\sinh^{-1}\left(\frac{1-\lambda}{\mu}\right) + \sinh^{-1}\left(\frac{1+\lambda}{\mu}\right)\right)\frac{x-1}{2} + \sinh^{-1}\left(\frac{1-\lambda}{\mu}\right)\right] \tag{17}$$

where the parameters λ and μ denote the location and width of the boundary layer, respectively.

The transformed Chebyshev points $\{g_{\lambda,\mu}(x_k)\}_{k=0}^{N}$ are clustered near the boundary layer location $x = \lambda$, and their density is determined by the boundary layer width μ. To address singularly perturbed problems with two boundary layers, Tee proposed a combined sinh transform,

$$\widetilde{g}_{\mu}(x) = \begin{cases} \frac{1}{2}\left[g_{-1,\mu}(2x+1) - 1\right], & x \in [-1, 0), \\ \frac{1}{2}\left[g_{1,\mu}(2x-1) + 1\right], & x \in [0, 1]. \end{cases} \tag{18}$$

All derivatives of the piecewise map $\widetilde{g}$ are continuous at $x = 0$, ensuring the preservation of spectral accuracy. For the reaction–diffusion type, the parameter in (18) is chosen as $\mu = 2\tau_0$.

2.4. Theoretical guidance for sinh transform parameter selection

While the sinh transform in Equations (17) and (18) provides a powerful tool for resolving boundary layers, its effectiveness hinges on appropriate parameter choices. To move beyond empirical selection, we derive scaling principles from the asymptotic boundary layer theory in Lemmas 3 and 4.

For convection-diffusion problems, the boundary layer at $x = 1$ has characteristic width:

$$\mu_{\text{BL}} = \frac{\varepsilon}{\beta} ln\left(\frac{|\beta - \omega(1)|}{\varepsilon}\right), \tag{19}$$

which depends on the reduced solution at the boundary $x = 1$. Since $\omega(1)$ is not available a priori, formula (19) cannot be used directly in an automated computational procedure.

To obtain a fully adaptive algorithm, we employ the practical formula,

$$\mu = \kappa \cdot \frac{\varepsilon}{|\beta|} \cdot ln\left(1 + \frac{1}{\varepsilon}\right) \kappa \in [0.8, 1.2], \tag{20}$$

which depends only on the known parameters ε and β. The choice $\kappa = 1.0$ is adopted throughout the numerical experiments of Section 4. This formula gracefully handles the $\varepsilon \to 0$ limit while avoiding singularities.

Formula (20) requires no knowledge of the solution. The factor κ provides a simple mechanism to compensate for the omitted constant $\ln(|\beta - \omega(1)|)$; numerical tests confirm that the resulting accuracy is comparable to that obtained with the theoretical width (19).

For reaction-diffusion problems, twin boundary layers occur with width:

$$\mu = \kappa\sqrt{\frac{\varepsilon}{c_0}}, \quad c_0 = \min(|c(0)|, |c(1)), \kappa \in [0.8, 1.2]. \tag{21}$$

These theoretical widths provide the natural scaling for the sinh transform parameter μ. The constants κ ensure sufficient grid points cluster within the boundary layer region.

Based on **Figure 1**, which displays the distribution of Chebyshev–Gauss–Lobatto and collocation points over the interval [1] for the model problem with $b(x) = 1 + x^2$ and $\kappa = 4, 6, 8$ a boundary layer at $x = 1$, the following observations are made: As the parameter κ decreases from 1.2 to 0.8, the collocation points become increasingly clustered near the right endpoint $x = 1$. For larger values of κ, the points remain more uniformly spaced, whereas for smaller κ a pronounced concentration occurs within the boundary-layer region. This redistribution is a direct consequence of the sinh-type coordinate transformation, which adaptively concentrates grid points where the solution exhibits sharp gradients, thereby enhancing numerical resolution and accuracy in capturing boundary-layer behavior.

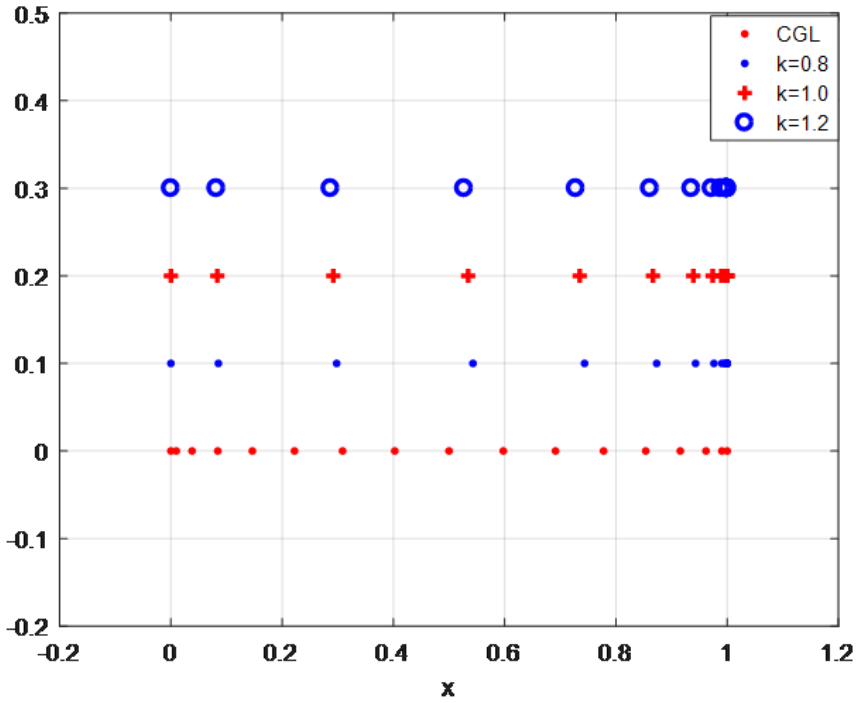

Figure 1. Distribution of collocation points for different values of κ.

This theoretical guidance addresses a key limitation in automated application of sinh transforms while maintaining the spectral accuracy demonstrated in our numerical experiments.

3. Enriched rational spectral collocation method with corrector functions

As demonstrated numerically in Section 4, the RSC-SSM method in the study of Li et al. [20] fails to maintain its high accuracy for variable-coefficient problems, owing to

its reliance on a constant-coefficient corrector. To overcome this limitation, we propose a fundamentally different ansatz derived directly from the variable-coefficient operator itself.

3.1. The convection–diffusion problem

Taking the convection–diffusion equation as an example, this section elaborates on the implementation and error estimation of ERSM-sinh.

Consider the following variable coefficient convection–diffusion problem:

$$\begin{cases} Lu := -\varepsilon u'' + b(1)u' = f(x), \quad x \in \Omega = (0,1), \\ u(0) = u_0, \quad u(1) = u_1. \end{cases} \tag{22}$$

The solution of problem (22) exhibits a boundary layer at $x = 1$. According to the singular perturbation analysis, the correction function is defined as,

$$\theta(x) = exp(\frac{b(1)}{\varepsilon}(x-1)). \tag{23}$$

which satisfies the homogeneous differential equation on (0,1):

$$-\varepsilon\theta'' + b(x)\theta' = 0, \quad x \in \Omega = (0,1). \tag{24}$$

Thus, the solution of problem (22) can be expressed as,

$$u(x) = z(x) + v(x), \tag{25}$$

where $v(x) = c_r\theta(x)$ is the singular component of (22), and the parameter c_r can be determined via an implicit method.

Substituting (25) into (22), and using (24), we obtain the system,

$$\begin{cases} -\varepsilon z''(x) + b(x)z'(x) + (b(x) - b(1))\theta'(x)c_r = f(x), \\ z(0) + c_r\theta(0) = u_0, \quad z(1) + c_r\theta(1) = u_1. \end{cases} \tag{26}$$

Let $\{t_k\}_{k=0}^N$ denote the Chebyshev-Gauss-Lobatto nodes. Using the linear trans--formation $x = \frac{t+1}{2}$, these nodes are mapped to the interval $[0,1]$. Discretizing (26) with the rational spectral method yields,

$$\begin{cases} (-\varepsilon D^{(2)} + BD^{(1)})w + \mathbf{a}_r c_r = F, \\ w_0 + c_r\theta(x_0) = u_0, \quad w_N + c_r\theta(x_N) = u_1, \end{cases} \tag{27}$$

where $w_k = z(x_k),\ F_k = f(x_k),\ B = \text{diag}(b(x_0), b(x_1), \cdots, b(x_N))$ is a diagonal matrix, $D^{(1)}$ and $D^{(2)}$ denote the first- and second-order differentiation matrices defined in (16), Moreover, we define the column vector $\mathbf{a}_r = (a_r(0), a_r(1), \cdots, a_r(N))^T$ with entries $a_r(k) = (b(x_k) - b(x_N))\theta'(x_k)$ for $k = 0, 1, \cdots, N$. The discrete system (26) can be written in the matrix-vector form,

$$\widehat{A} \cdot \widehat{W} = \widehat{F} \tag{28}$$

where $\widehat{A}$ is a $(N+2)\times(N+2)$ matrix such that,

$$\widehat{A}=\begin{bmatrix} 1 & 0 & \cdots & 0 & 0 & \theta(x_0) \\ & & & & & a_\gamma(1) \\ & & \widetilde{A} & & & \vdots \\ & & & & & a_\gamma(N) \\ 0 & 0 & \cdots & 0 & 1 & \theta(x_N) \end{bmatrix}, \widehat{W}=\begin{bmatrix} w_0 \\ w_1 \\ \vdots \\ w_N \\ c_\gamma \end{bmatrix}, \widehat{F}=\begin{bmatrix} u_0 \\ f_1 \\ \vdots \\ f_N \\ u_1 \end{bmatrix}$$

Consequently, the $N\times(N+1)$ block matrix $\widetilde{A}$ is given by $\widetilde{A}=A(2:N+1,1:N+1)$, where,

$$A=-\varepsilon D^{(2)}+BD^{(1)}$$

Solving (28) yields the numerical solution of problem (22),

$$u(x_k)\approx u_k=\widehat{W}_k+\widehat{W}_{N+1}\theta(x_k),\quad k=0,1,2,\cdots,N. \tag{29}$$

The aforementioned algorithm is termed the Enriched Rational Spectral Method (ERSM). When the collocation points *x* are clustered toward the boundary layer using the sinh transformation (17), this enhanced version is referred to as ERSM-sinh.

For the general case (1) with $c(x)\neq 0$ and $b(x)\geq\beta>0$, the solution exhibits a boundary layer at $x=1$. Singular perturbation analysis shows that the correction function $\theta(x)$, defined in (23) for the convection-diffusion case, remains applicable and satisfies the corresponding homogeneous Equation (24). Substituting the ansatz $u(x)=z(x)+c_r\theta(x)$ into (1) yields the system,

$$\begin{cases} -\varepsilon z^{''}(x)+b(x)z^{'}(x)+c(x)z(x)+(b(x)-b(1))\theta^{'}(x)c_r+c(x)\theta(x)c_r=f, \\ z(0)+c_r\theta(0)=u_0,\quad z(1)+c_r\theta(1)=u_1. \end{cases} \tag{30}$$

Discretizing (30) similarly leads to the algebraic system:

$$\begin{cases} (-\varepsilon D^{(2)}+BD^{(1)}+C)w+\boldsymbol{a}_r c_r=F, \\ w_0+c_r\theta(x_0)=u_0,\quad w_N+c_r\theta(x_N)=u_1. \end{cases} \tag{31}$$

Here, $C=diag(c(x_0),c(x_1),\cdots,c(x_N))$is the reaction term matrix, and $\boldsymbol{a}_r=(a_r(0),a_r(1),\cdots,a_r(N))^\top$is the correction vector with components,

$$a_r(k)=(b(x_k)-b(x_N))\theta^{'}(x_k)+c(x_k)\theta(x_k),\quad k=0,1,\cdots,N.$$

The remaining notation follows that established in (27).

$$A=-\varepsilon D^{(2)}+BD^{(1)}+C, \tag{32}$$

is the full discrete operator matrix.

3.2. The reaction–diffusion problem

When considering the problem (1) with $b(x) \equiv 0$, the system is referred to as being of reaction–diffusion type.

$$\begin{cases} Lu := -\varepsilon u'' + c(x)u = f(x), \quad x \in \Omega = (0,1), \\ u(0) = u_0, u(1) = u_1. \end{cases} \tag{33}$$

This problem exhibits boundary layers at both endpoints $x = 0$ and $x = 1$. Singular perturbation analysis shows that,

$$\theta_l(x) = e^{-\frac{\sqrt{c(0)}}{\sqrt{\varepsilon}}x}, \quad \theta_r(x) = e^{\frac{\sqrt{c(1)}}{\sqrt{\varepsilon}}(x-1)}. \tag{34}$$

Thus, the solution of (32) can be expressed as,

$$u(x) = z(x) + c_l\theta_l(x) + c_r\theta_r(x), \tag{35}$$

where $v(x) = c_l\theta_l(x) + c_r\theta_r(x)$ is the singular component, and the coefficients c_l, c_r can be determined via an implicit method.

Substituting the ansatz (35) into (33), we obtain the coupled system:

$$\begin{cases} -\varepsilon z''(x) + c(x)z(x) + c_l(c(x) - c(0))\theta_l(x) + c_r(c(x) - c(1))\theta_r(x) = f(x), \\ z(0) + c_l\theta_l(0) + c_r\theta_r(0) = u_0, \quad z(1) + c_l\theta_l(1) + c_r\theta_r(1) = u_1. \end{cases} \tag{36}$$

Let $\{t_k\}_{k=0}^N$ denote the Chebyshev- Gauss-Lobatto nodes, mapped to the interval [1] via the linear transformation $x = \frac{t+1}{2}$. Discretizing the system (36) using the rational spectral method yields:

$$\begin{cases} (-\varepsilon D^{(2)} + C)w + \boldsymbol{a}_l c_l + \boldsymbol{a}_r c_r = F, \\ w_0 + c_l\theta_l(x_0) + c_r\theta_r(x_0) = u_0, \quad w_N + c_l\theta_l(x_N) + c_r\theta_r(x_N) = u_1, \end{cases} \tag{37}$$

where $C = diag(c(x_0), c(x_1), \cdots, c(x_N))$ is the reaction coefficient matrix, $D^{(1)}$ and $D^{(2)}$ are the differential matrices defined in (16), and $\boldsymbol{a}_l$, $\boldsymbol{a}_r$ are column vectors defined as follows:

$$\begin{aligned} \boldsymbol{a}_l &= (a_l(0), a_l(1), \cdots, a_l(N))^T, \quad a_l(k) = (c(x_k) - c(x_0))\theta_l(x_k), \\ \boldsymbol{a}_r &= (a_r(0), a_r(1), \cdots, a_r(N))^T, \quad a_r(k) = (c(x_k) - c(x_N))\theta_r(x_k). \end{aligned}$$

The matrix form of system (37) maintains the structure of (28), the coefficient matrix of (28) has the following form,

$$\widehat{\mathbf{A}} = \begin{bmatrix} 1 & \cdots & 0 & \theta_l(x_0) & \theta_\gamma(x_0) \\ & & & a_l(0) & a_\gamma(0) \\ & A & & \vdots & \vdots \\ & & & a_l(N) & a_\gamma(N) \\ 0 & \cdots & 1 & \theta_l(x_N) & \theta_\gamma(x_N) \end{bmatrix}, \widehat{\mathbf{W}} = \begin{bmatrix} w_0 \\ \vdots \\ w_N \\ c_l \\ c_r \end{bmatrix}, \widehat{\mathbf{F}} = \begin{bmatrix} u_0 \\ f_0 \\ \vdots \\ f_N \\ u_1 \end{bmatrix} \tag{38}$$

where $w_k = z(x_k)$, and $f_k = f(x_k)$, $k = 0, 1, 2, \cdots, N$, the $(N+1) \times (N+1)$

matrix A is given by $A = -\varepsilon D^{(2)} + C$. The approximate solution of problem (33) in the following form can be obtained by solving the linear system of equations in the form of Equation (28)

$$u^N(x_k) \approx u_k = \widehat{W}_k + \widehat{W}_{N+1}\theta_l(x_k) + \widehat{W}_{N+2}\theta_r(x_k), \quad k = 0, 1, \cdots, N. \tag{39}$$

3.3. Error analysis

In this subsection, we establish an error estimate for the ERSM-sinh method (39) applied to singularly perturbed reaction-diffusion problems.

Theorem 3. *Suppose that after discretizing the differential problem (31) using the Chebyshev method at the Chebyshev-Gauss-Lobatto nodes, we obtain a discrete matrix of the form,*

$$\widehat{A} = \begin{bmatrix} 1 & \cdots & 0 & \theta_l(x_0) & \theta_r(x_0) \\ & & & a_l(0) & a_r(0) \\ & A & & \vdots & \vdots \\ & & & a_l(N) & a_r(N) \\ 0 & \cdots & 1 & \theta_l(x_N) & \theta_r(x_N) \end{bmatrix},$$

where the symbols take values as in Section 3.3. Then, the matrix $\widehat{A}$ is invertible.

Proof. It suffices to show that the homogeneous equation $\widehat{A} \cdot \widehat{W} = 0$ has only the trivial solution. This system is equivalent to:

$$\begin{cases} w_0 + c_l\theta_l(x_0) + c_r\theta_r(x_0) = 0, \\ A\boldsymbol{w} + \boldsymbol{a}_l c_l + \boldsymbol{a}_r c_r = 0, \\ w_N + c_l\theta_l(x_N) + c_r\theta_r(x_N) = 0, \end{cases}$$

where $\boldsymbol{w} = [w_0, w_1, \ldots, w_N]^T$. □

Defining the discrete function,

$$u_k = w_k + c_l\theta_l(x_k) + c_r\theta_r(x_k), \quad k = 0, 1, \ldots, N,$$

and the boundary conditions $u_0 = 0, u_N = 0$. Furthermore, by construction of the corrector functions θ_l and θ_r and the vectors $\boldsymbol{a}_l, \boldsymbol{a}_r$, the second equation implies that the discrete function $\boldsymbol{u} = [u_0, \cdots, u_N]^T$ satisfies,

$$(-\varepsilon D^{(2)} + C)\boldsymbol{u} = 0.$$

Since the discrete operator,

$$A = (-\varepsilon D^{(2)} + C),$$

is invertible for this well-posed problem [30], we conclude that $\boldsymbol{u} = 0$. The uniqueness of the decomposition for the continuous problem then implies $c_l = c_r = 0$ and thus, $\boldsymbol{w} = 0$. Therefore, $\widehat{W} = 0$, proving that $\widehat{A}$ is invertible.

In the following analysis, we assume that the coefficients $b(x), c(x)$ and the source term $f(x)$ are smooth on [1], which allows the rational spectral method to achieve exponential convergence after the sinh-transform is applied.

Theorem 4. *Let $u(x_i)$ and $u^N(x_i)$ be the exact and numerical solutions of the original problem (33), respectively. Then, we have,*

$$\varepsilon\|e^{'}\|^2_{L^2(0,1)} + \frac{\alpha}{2}\|e\|^2_{L^2(0,1)} = \mathbb{O}(\rho^{-N})$$

where ρ is the sum of the lengths of the major and minor axes of the ellipse C_ρ with $foci \pm 1$ $(\rho > 1)$.

Proof. Let $e(x) = u(x) - u^N(x)$, the error $e(x)$ satisfies,

$$\begin{cases} -\varepsilon e^{''} + c(x)e = f(x) - f_N(x), \quad x \in \Omega = (0,1), \\ e(0) = u(0) - u_N(0) = 0, \quad e(1) = u(1) - u_N(1) = 0, \end{cases}$$

where $f_N(x)$ is the rational spectral approximation of $f(x)$. Multiplying both sides by $e(x)$ and integrating by parts over $[0,1]$ yields,

$$\varepsilon \int_0^1 (e^{'})^2 dx + \int_0^1 ((x)e^2 dx = \int_0^1 (f(x) - f_N(x))e dx. \square$$

Applying the Cauchy–Schwarz inequality gives,

$$\varepsilon \int_0^1 (e^{'})^2 dx + \alpha \int_0^1 e^2 dx \le \|f - f_N\|_{L^2(0,1)} \|e\|_{L^2(0,1)}$$

An application of Young's inequality then yields,

$$\begin{aligned} \varepsilon \left\|e^{'}\right\|^2_{L^2(0,1)} + \alpha \|e\|^2_{L^2(0,1)} &\le \|f - f_N\|_{L^2(0,1)} \|e\|_{L^2(0,1)} \\ &\le \tfrac{1}{2\alpha} \|f - f_N\|^2_{L^2(0,1)} + \tfrac{\alpha}{2} \|e\|^2_{L^2(0,1)}. \end{aligned}$$

Then,

$$\varepsilon\|e^{'}\|^2_{L^2(0,1)} + \frac{\alpha}{2}\|e\|^2_{L^2(0,1)} \le \frac{1}{2\alpha}\|f - f_N\|^2_{L^2(0,1)}.$$

From the approximation theorem for rational interpolation, it follows that:

$$\varepsilon\|e^{'}\|^2_{L^2(0,1)} + \frac{\alpha}{2}\|e\|^2_{L^2(0,1)} = \mathbb{O}(\rho^{-N}).$$

Consequently, the rational spectral method with the singularity-separated technique achieves nearly spectral accuracy.

The error bound (39) remains valid for variable coefficients provided that the composite function $u \circ g^{-1}$ retains sufficient regularity in the mapped domain. The key requirement is that the coefficients $b(x), c(x), f(x)$ allow u to be analytically continued to a complex neighborhood of [1]. In practice, if the coefficients are themselves analytic, their variability does not destroy the exponential convergence—it merely influences the size of the ellipse ρ in Theorem 2, and hence the constant in front of the exponential decay. Numerical evidence supporting this claim is provided in Section 4, where problems with non-constant $b(x)$ and $c(x)$ still exhibit spectral accuracy.

The error analysis presented in Theorem 4 relies on the analyticity of the exact solution $u(x)$ in the complex plane. When the coefficients $b(x)$ and $c(x)$ in (1) are variable but analytic on $[0,1]$ and can be analytically continued to a neighborhood in

the complex plane, the composition $u^{\circ}\ g^{-1}$ remains analytic within an ellipse , and Theorem 2 guarantees spectral convergence.

4. Numerical experiments

We validate the accuracy and efficiency of the proposed ERSM-sinh method by applying it to several singularly perturbed boundary value problems with known analytical solutions. The maximum relative error of the solution is given by,

$$e_{\infty} = \frac{\|u_N - u\|_{\infty}}{\|u_E\|_{\infty}} \tag{40}$$

where u_N and u are the numerical and exact solutions, respectively. All computations were performed in MATLAB R2016b on a PC with AMD Ryzen 7 5800H processor (3.20 GHz) running Windows 11.

In all numerical examples presented in this paper, the parameter μ of the single-layer sinh transformation (17) is determined automatically via formula (20) with k = 1.0, while the parameter μ of the two-layer combined sinh transformation (18) is determined automatically via formula (21) with k = 1.0. This approach ensures a fully adaptive numerical solution without requiring any manual parameter tuning.

Example 1. *Consider the variable coefficient singularly perturbed convection-diffusion problem (with* $c = 0$*):*

$$\begin{cases} -\varepsilon u'' + (1+x^2)u' = f(x), \quad 0 < x < 1, \\ u(0) = 1/2, \quad u(1) = -1, \end{cases}$$

where,

$$f(x) = \frac{2e^{\frac{2}{\varepsilon}(x-1)}(x^2-1)}{\varepsilon e^{-\frac{2}{\varepsilon}} - 1} - \frac{1+x^2}{2}.$$

The exact solution is,

$$u(x) = \frac{e^{\frac{2}{\varepsilon}(x-1)} - 1}{e^{-\frac{2}{\varepsilon}} - 1} - \frac{1+x}{2}.$$

Since $b(x) = 1 + x^2 > 0$ *on* $(0, 1)$*, a boundary layer occurs at* $x = 1$.

The corrector is taken as,

$$\theta(x) = e^{\frac{b(1)}{\varepsilon}(x-1)} = e^{\frac{2}{\varepsilon}(x-1)},$$

which satisfies,

$$-\varepsilon\theta''(x) + b(1)\theta(x) = 0.$$

We compare the standard spectral method (SM), the RSCAT method [18], the ESM [21], the RSC-SSM [20], and the Enriched Rational Spectral Method combined with the sinh transformation (ERSM-sinh). **Figure 2** compares the exact solution with the numerical results obtained by ESM and ERSM-sinh. Both schemes reproduce the overall behavior of the solution. However, a closer inspection reveals that ERSM-sinh follows the exact curve more closely inside the boundary-layer region, demonstrating the advantage of the sinh-transformed collocation grid. **Table 1** lists the maximum

relative errors L_∞ for different values of the perturbation parameter ε and the number of collocation points N. When ε is moderately large (e.g., 10^{-1}), the standard spectral method already attains machine-precision accuracy. Under such conditions, the boundary layer is mild, so the additional enrichment or transformation used in the other methods where the enriched methods does not improve accuracy and can even introduce slightly larger errors. This observation is consistent with the error profiles displayed in **Figure 3**, where the enriched methods show no benefit for large ε. As ε decreases, the boundary layer becomes sharper and more localized. **Figure 4a,b** illustrates how the pointwise errors of the four methods evolve when ε is reduced from 10^{-2} to 10^{-4}. With a narrower layer, the standard spectral method (SM) loses accuracy because its uniformly spaced collocation points cannot resolve the steep gradient. In contrast, the enriched methods—especially ERSM-sinh—maintain high precision by concentrating collocation points near the boundary via the sinh transformation and by incorporating a problem-specific corrector function. The results in **Table 1** confirm that for small ε (e.g., 10^{-4} and 10^{-6}), ERSM-sinh achieves errors that are several orders of magnitude smaller than those of SM, RSCAT, ESM, and RSC-SSM.

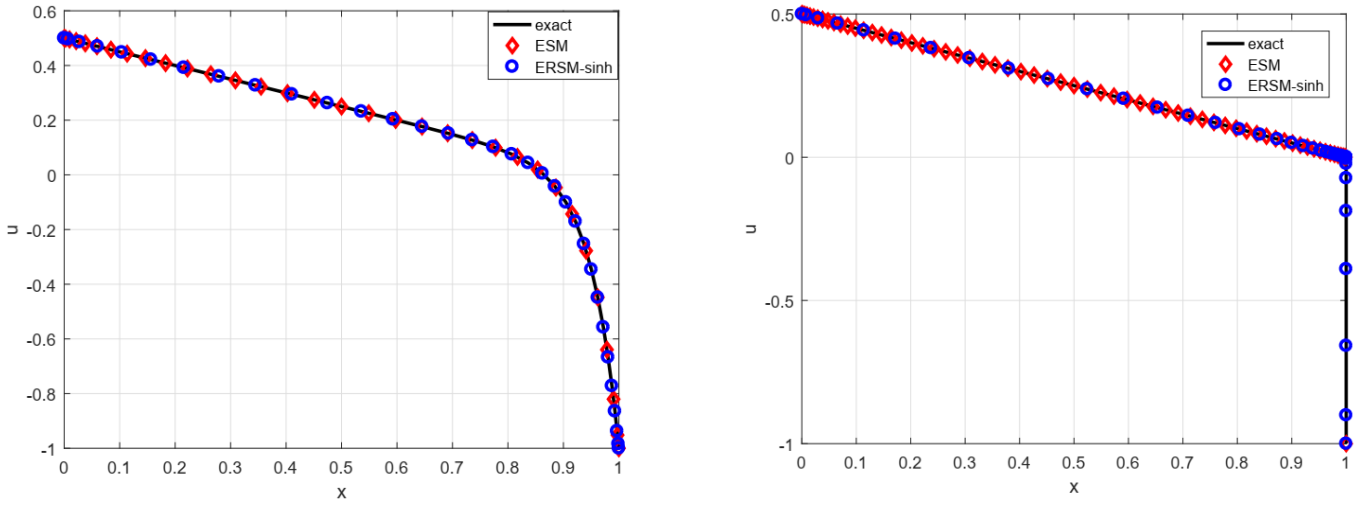

(a) $\varepsilon = 10^{-1}, N = 32$. **(b)** $\varepsilon = 10^{-6}, N = 64$.

Figure 2. Comparison of the ESM and ERSM-sinh numerical solutions with the exact solution.

Table 1. Comparison of the maximum relative errors L_∞ for Example 1.

ε	N	SM	RSCAT	ESM	RSC-SSM	ERSM-sinh
10^{-1}	32	8.72×10^{-15}	1.83×10^{-8}	6.02×10^{-5}	9.25×10^{-2}	1.75×10^{-5}
	48	2.26×10^{-14}	3.73×10^{-9}	5.18×10^{-6}	1.13×10^{-2}	1.08×10^{-7}
10^{-2}	32	1.50×10^{-3}	1.74×10^{-6}	1.83×10^{-15}	6.11×10^{-3}	4.49×10^{-14}
	48	1.68×10^{-6}	7.93×10^{-9}	8.44×10^{-15}	7.48×10^{-3}	3.83×10^{-11}
	64	2.11×10^{-10}	1.86×10^{-9}	3.58×10^{-11}	8.64×10^{-3}	3.77×10^{-8}
10^{-4}	32	6.87×10^{0}	1.91×10^{-4}	3.47×10^{-16}	4.34×10^{-5}	8.28×10^{-15}
	48	2.48×10^{0}	4.35×10^{-9}	1.05×10^{-15}	5.33×10^{-5}	2.05×10^{-11}
	64	1.25×10^{0}	9.31×10^{-10}	7.22×10^{-16}	6.15×10^{-5}	1.28×10^{-9}

Table 1. *Cont.*

ε	N	SM	RSCAT	ESM	RSC-SSM	ERSM-sinh
10^{-6}	32	$6.49 \times 10^{+2}$	1.76×10^{0}	1.47×10^{-15}	8.42×10^{-7}	5.90×10^{-16}
	48	$2.88 \times 10^{+2}$	8.91×10^{-4}	5.00×10^{-16}	4.28×10^{-7}	6.11×10^{-16}
	64	$1.62 \times 10^{+2}$	2.74×10^{-7}	9.49×10^{-16}	5.03×10^{-7}	1.33×10^{-16}

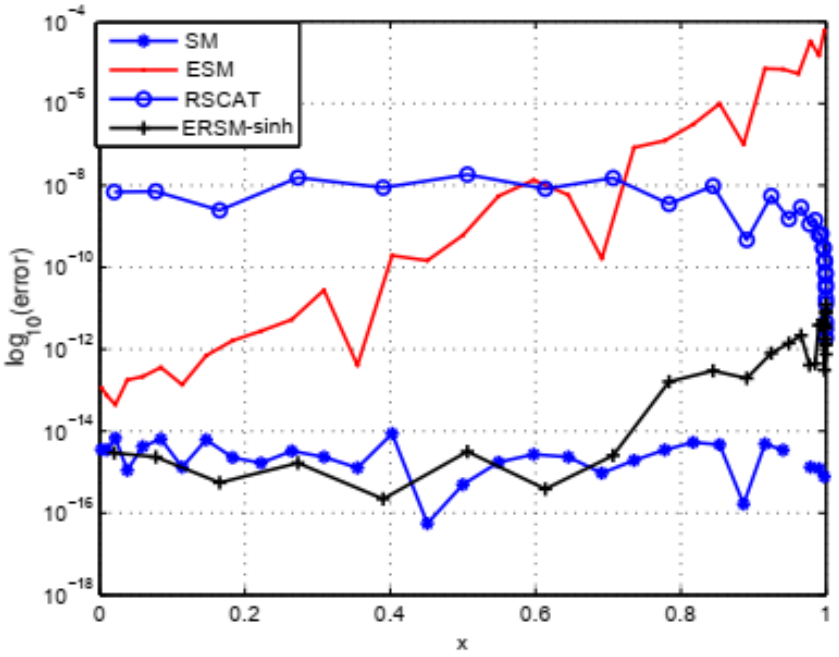

Figure 3. The pointwise errors for the four methods with $\varepsilon = 10^{-1}, N = 32$.

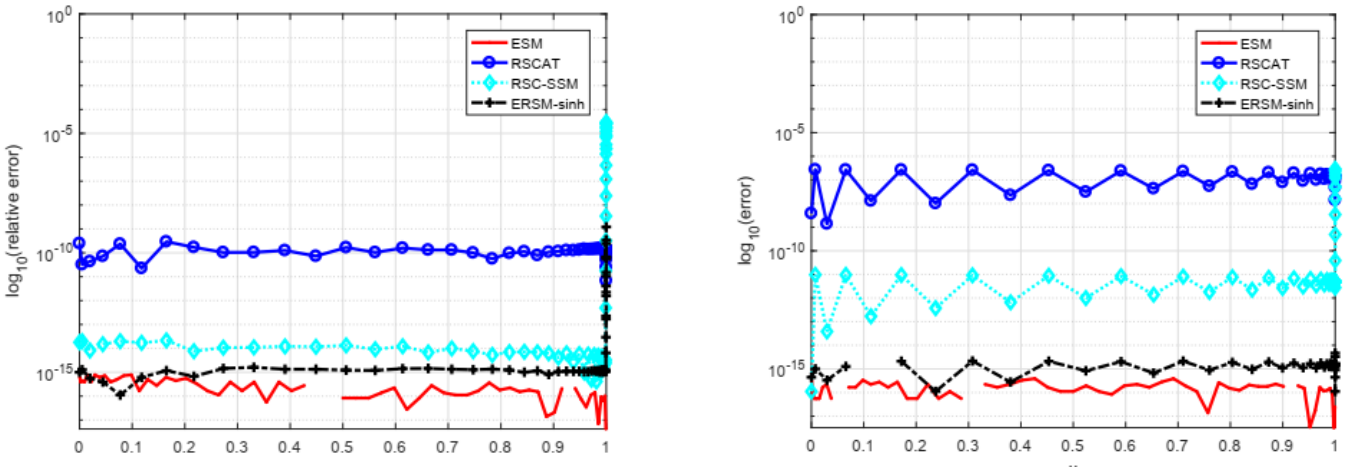

(a) $\varepsilon = 10^{-4}, N = 64$*. **(b)** $\varepsilon = 10^{-6}, N = 64$*.

Figure 4. The pointwise errors for the four methods.

Note: [*]: The discontinuities observed in the logarithmic error plots originate from computationally zero relative errors, which yield an undefined logarithm.

Figure 5 plots the maximum relative error versus the number of collocation points N for a fixed small perturbation parameter ε. The error of ERSM-sinh decays most rapidly, demonstrating its superior spectral convergence rate. In contrast, the errors of the standard spectral method (SM) and the RSC-SSM method quickly stagnate as N

increases, indicating that grid refinement alone does not substantially improve their accuracy when a sharp boundary layer is present. These observations underline that ERSM-sinh maintains robust exponential convergence even for very small ε, whereas the other methods suffer from a loss of convergence efficiency due to inadequate resolution of the thin layer.

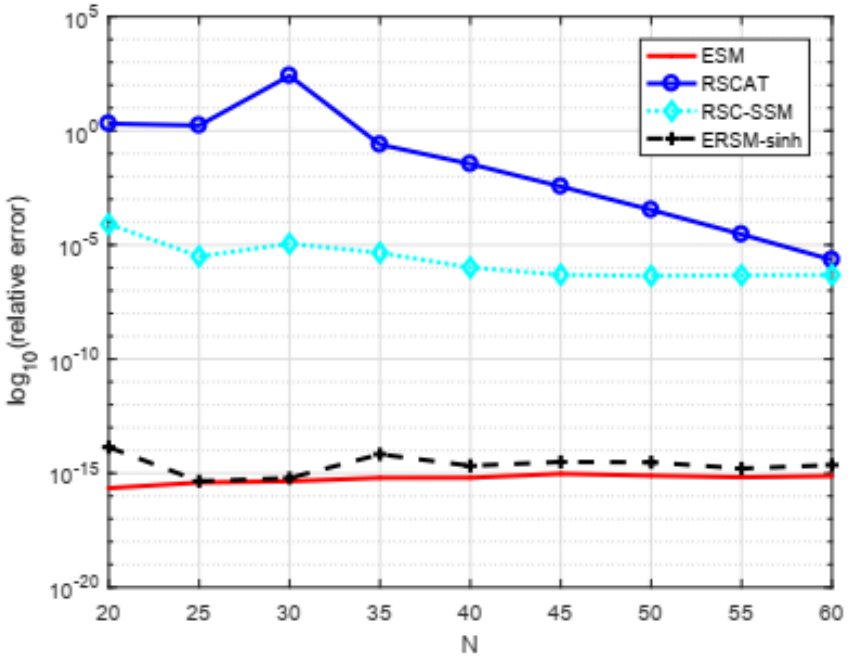

Figure 5. The convergence rate in Example 1 with $\varepsilon = 10^{-6}$.

The computational cost of each method is presented in **Table 2**, which lists the CPU times for Example 1 with $N = 32$ and 48. The five schemes—SM, RSCAT, ESM, RSC-SSM, and ERSM-sinh—exhibit very similar run-times. This confirms that the additional steps introduced by the enrichment and the sinh-transformation do not impose a significant overhead, making the proposed ERSM-sinh method computationally competitive.

Table 2. Computational time comparison between different models for Example 1.

ε	N	SM (s)	RSCAT (s)	ESM (s)	RSC-SSM (s)	ERSM-sinh (s)
10^{-2}	32	0.00394	0.00418	0.00415	0.00412	0.00423
10^{-4}	48	0.00510	0.00524	0.00539	0.00520	0.00546

Although ESM occasionally shows smaller point-wise errors than ERSM-sinh in **Table 1** (e.g., 7.22×10^{-16} vs. 1.28×10^{-9} for $\varepsilon = 10^{-4}$ and $N = 64$), this does not imply superior performance. **Figure 6** provides a clearer insight: because ESM employs a uniform or nearly uniform collocation grid, it places too few points inside the thin boundary layer. Consequently, even when its maximum error appears small, ESM cannot faithfully represent the fine-scale structure of the solution within the layer. The error distribution in **Figure 4b** confirms that ESM fails to capture the sharp gradient near the boundary, leading to a distorted numerical profile in that region.

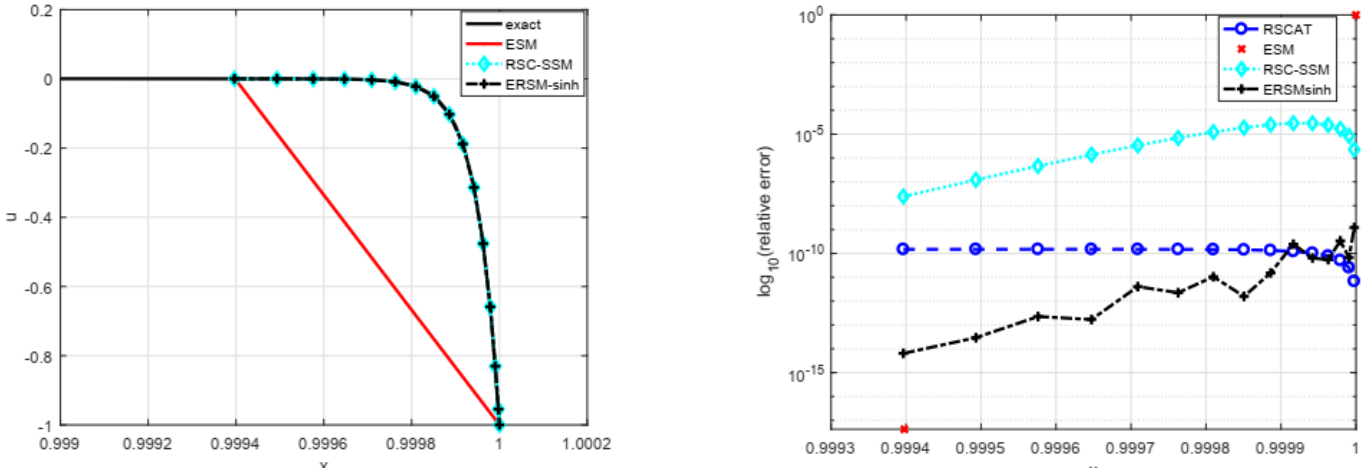

(a) Solution. **(b) Pointwise error.**

Figure 6. Solutions and pointwise errors on the boundary layer region in Example 1 with $\varepsilon = 10^{-4}, N = 64$.

In contrast, the sinh-transformed grid used in ERSM-sinh automatically clusters collocation points near the boundary where the layer is located. This adaptive point distribution, illustrated in **Figure 4a**, allows the method to resolve the steep gradient accurately. Thus, while ESM may occasionally yield a marginally lower global error in some cases, its inability to represent the layer's detailed behavior—evident in the pointwise error plots—limits its reliability for singularly perturbed problems with sharp layers. The proposed ERSM-sinh scheme, by concentrating resolution where it is most needed, achieves a more physically faithful and robust representation of the boundary-layer structure, which is essential for accuracy when the perturbation parameter is small.

Example 2. *Consider the following singularly perturbed reaction--diffusion (i.e., $b(x) = 0$) problem with variable coefficients:*

$$\begin{cases} -\varepsilon u'' + (1+x)^2 u = f(x), \quad 0 < x < 1, \\ u(0) = 0, \quad u(1) = 0, \end{cases}$$

where,

$$f(x) = (1+x)^2 + e^{-\frac{x}{\sqrt{\varepsilon}}}(2\sqrt{\varepsilon} + x(-2+x+x^2)) + e^{\frac{2(x-1)}{\sqrt{\varepsilon}}}(4\sqrt{\varepsilon} - x(-3+2x+x^2)).$$

The exact solution can be expressed as,

$$u(x) = 1 + (x-1)e^{-\frac{x}{\sqrt{\varepsilon}}} - xe^{\frac{2(x-1)}{\sqrt{\varepsilon}}}.$$

This problem has two boundary layer regions, located at the two endpoints of the underlying interval $[0, 1]$. According to the singular perturbation analysis, the corrector functions at the left and right endpoints are constructed as,

$$\theta_l(x) = e^{-\frac{\sqrt{c(0)}}{\sqrt{\varepsilon}}x} = e^{-\frac{1}{\sqrt{\varepsilon}}x}, \quad \theta_r(x) = e^{\frac{\sqrt{c(1)}}{\sqrt{\varepsilon}}(x-1)} = e^{\frac{2}{\sqrt{\varepsilon}}(x-1)}.$$

For the reaction–diffusion singularly perturbed problem featuring twin boundary

layers, the computational times listed in **Table 3** indicate that all five methods incur comparable CPU costs, which confirms that the enrichment procedure and the grid transformation do not introduce significant overhead. **Table 4** lists the maximum relative errors obtained under various values of the perturbation parameter ε and the number of collocation points N. When ε is relatively large (e.g., 10^{-2}), the solution is essentially smooth and no sharp boundary layer develops.

Table 3. Computational time comparison between different models for Example 2.

ε	N	SM (s)	RSCAT (s)	ESM (s)	RSC-SSM (s)	ERSM-sinh (s)
10^{-4}	40	0.00395	0.00410	0.00408	0.00412	0.00427
10^{-8}	60	0.00602	0.00624	0.00614	0.00610	0.00643

Table 4. Comparison of the maximum relative errors L_∞ for Example 2.

ε	N	SM	RSCAT	ESM	RSC-SSM	ERSM-sinh
10^{-2}	20	1.43×10^{-9}	2.34×10^{-5}	3.09×10^{-5}	3.55×10^{-2}	5.29×10^{-6}
	40	2.97×10^{-15}	1.16×10^{-5}	6.86×10^{-3}	3.58×10^{-2}	3.83×10^{-7}
10^{-4}	20	4.24×10^{-3}	3.22×10^{-5}	7.94×10^{-5}	4.65×10^{-2}	2.84×10^{-7}
	40	1.52×10^{-5}	1.12×10^{-6}	3.62×10^{-8}	4.09×10^{-3}	1.38×10^{-8}
	60	3.70×10^{-10}	1.80×10^{-7}	4.56×10^{-2}	4.12×10^{-3}	2.03×10^{-9}
10^{-6}	20	1.70×10^{-2}	4.17×10^{-4}	2.66×10^{-5}	3.71×10^{-4}	1.35×10^{-7}
	40	2.51×10^{-2}	7.87×10^{-7}	2.27×10^{-5}	4.19×10^{-4}	7.24×10^{-10}
	60	4.58×10^{-3}	1.21×10^{-7}	9.83×10^{-6}	4.17×10^{-4}	9.86×10^{-11}
10^{-8}	20	1.96×10^{-4}	2.72×10^{-3}	3.92×10^{-8}	4.17×10^{-5}	2.41×10^{-7}
	40	3.14×10^{-3}	9.46×10^{-7}	6.31×10^{-7}	4.18×10^{-5}	2.16×10^{-10}
	60	1.45×10^{-2}	4.65×10^{-8}	2.49×10^{-6}	4.17×10^{-5}	1.11×10^{-11}
10^{-10}	20	1.96×10^{-6}	3.76×10^{-3}	3.92×10^{-11}	3.13×10^{-6}	9.82×10^{-8}
	40	3.15×10^{-5}	4.68×10^{-5}	6.30×10^{-10}	4.20×10^{-6}	1.10×10^{-10}
	60	1.60×10^{-4}	1.71×10^{-8}	3.19×10^{-9}	4.09×10^{-6}	2.87×10^{-10}

In this regime, the standard spectral method (SM) yields the highest accuracy, whereas the enriched methods (ESM and ERSM-sinh) produce slightly larger errors. For smooth solutions, the additional collocation points that RSCAT and ERSM-sinh concentrate near the endpoints are unnecessary; they can even degrade the overall precision, as is visually evident in **Figure 7**.

The convergence behavior for a fixed ε is displayed in **Figure 8**. ERSM-sinh exhibits a rapid, monotonic decrease in the maximum error as the number of collocation points N increases, achieving the highest convergence rate among all the methods. In contrast, RSCAT shows initial improvement that quickly stagnates with increasing N, while the error of ESM actually rises, indicating a lack of consistent convergence. The RSC-SSM scheme maintains an almost constant error level regardless of N, revealing its limited suitability for variable-coefficient problems with sharp layers.

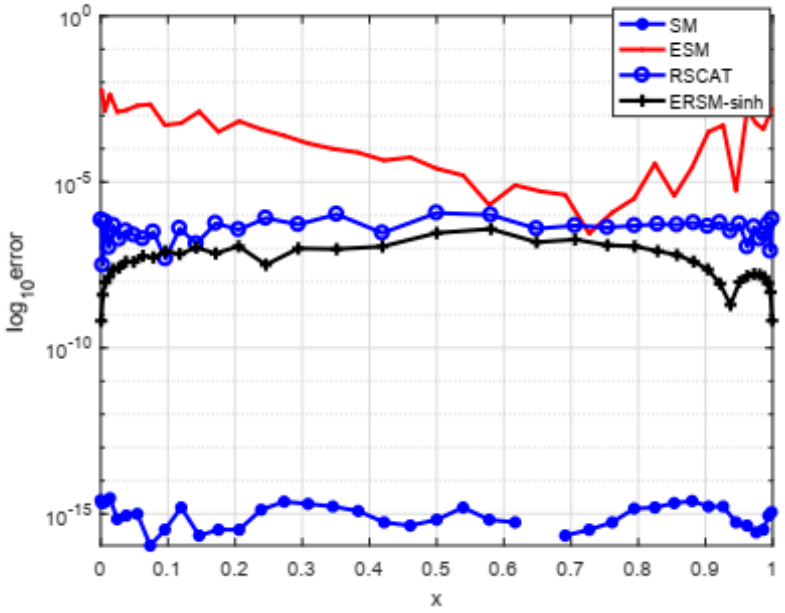

Figure 7. The pointwise errors of Example 2 with $\varepsilon = 10^{-2}, N = 40$*.

Note: [*]: The discontinuities observed in the logarithmic error plots originate from computationally zero relative errors, which yield an undefined logarithm.

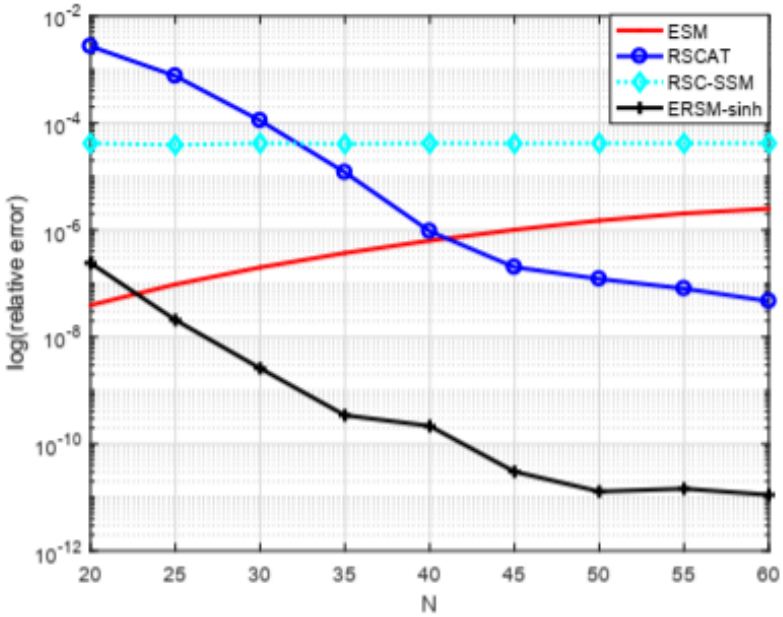

Figure 8. The convergence rate in Example 2 with $\varepsilon = 10^{-8}$.

The evolution of the boundary layer as the perturbation parameter decreases is clearly shown in **Figure 9**. With diminishing ε, the layer becomes increasingly thin and localized at the endpoints. To resolve such sharp gradients, the sinh transformation is applied, which maps the original Chebyshev collocation points to a new set that clusters densely near the singular points of the solution. As a consequence, both RSCAT and ERSM-sinh place a high density of nodes inside the layers, leading to a significant improvement in accuracy. Notably, ERSM-sinh outperforms RSCAT in capturing the fine-scale structure of the layer, as evident from the smaller pointwise errors in **Figure 9a,b**. This enhanced resolution stems from the enriched basis functions that are

tailored to the layer behavior.

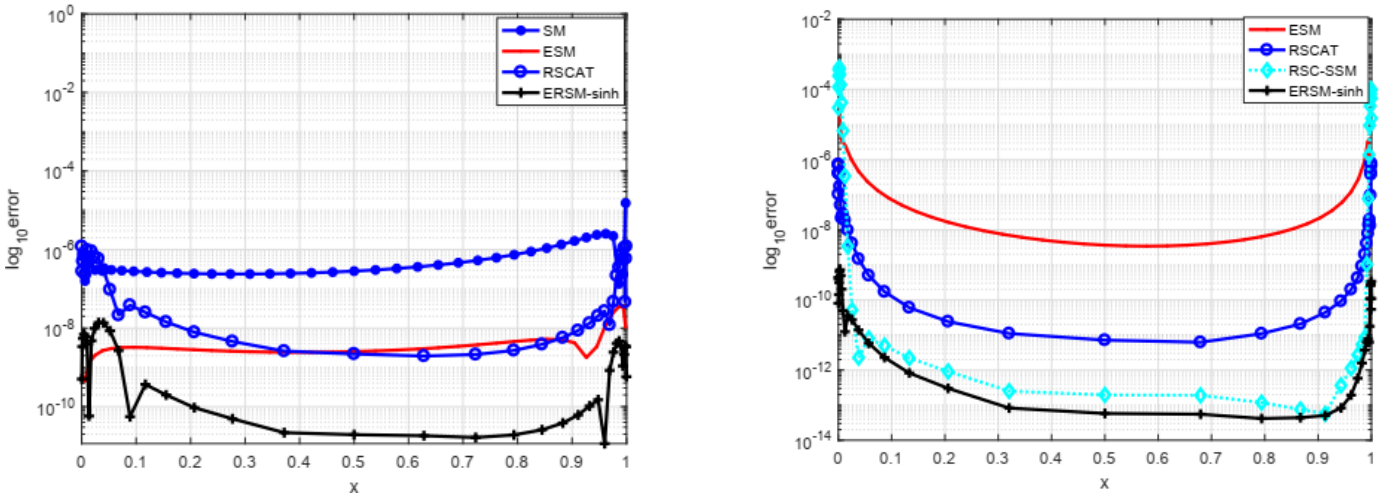

(a) $\varepsilon = 10^{-4}, N = 40$. **(b)** $\varepsilon = 10^{-6}, N = 40$.

Figure 9. The pointwise errors of Example 2.

To further insight into the ability of each method to capture the internal structure of the boundary layer, **Figure 10** compares the exact solution, the corresponding numerical approximations, the corresponding pointwise errors in the vicinity of the left boundary. Although ESM may occasionally produce a somewhat lower global error for particular choices of N and ε, its uniform collocation grid does not allocate enough points within the thin layer. As a result, ESM fails to resolve the steep gradient accurately, leading to a visibly distorted numerical profile near the boundary, as illustrated in **Figure 10b**. An analogous shortcoming is observed at the right endpoint. In contrast, the sinh-transformed grid employed by ERSM-sinh adaptively clusters collocation points near both boundaries, enabling the method to reproduce the fine-scale details of the layer and to deliver a numerically faithful representation of the solution across the entire domain.

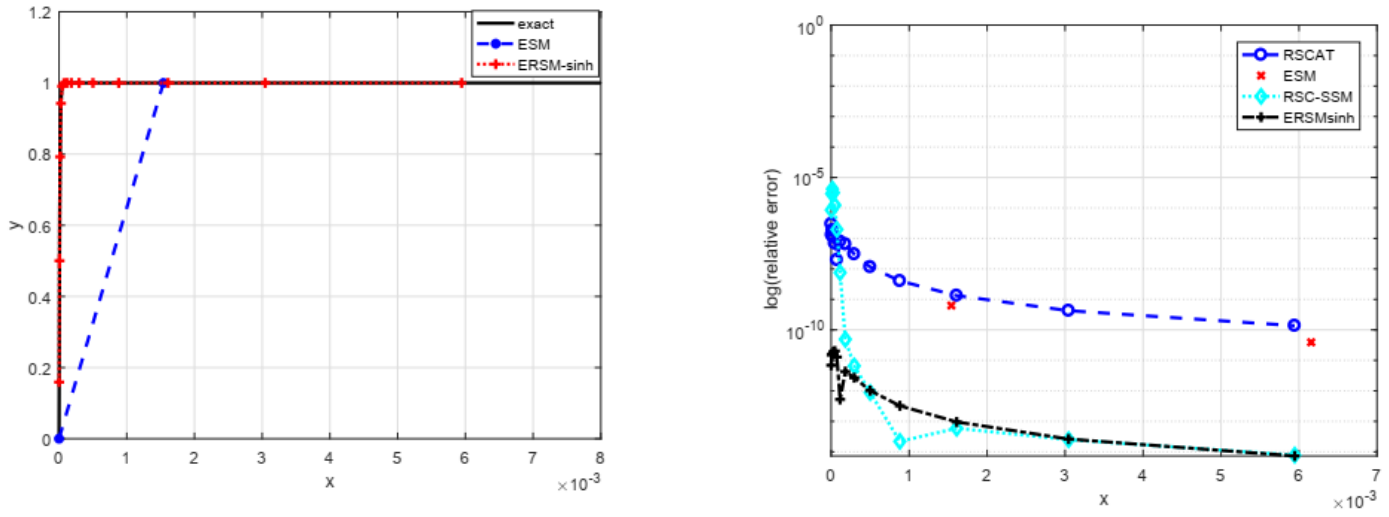

(a) Solution. **(b) Pointwise error.**

Figure 10. Solutions and pointwise errors on the boundary layer region in Example 2 with $\varepsilon = 10^{-10}, N = 40$.

The results presented in **Figures 7–9** demonstrate that the proposed ERSM-sinh

method combines an adaptive grid (via the sinh transformation) with an enriched basis to achieve high resolution inside boundary layers, superior convergence rates, and robust accuracy even for very small perturbation parameters. This makes it a highly effective and reliable approach for singularly perturbed reaction–diffusion problems with twin boundary layers.

This problem is also solved using two well-established reference methods: an asymptotic boundary layer approach [31], an exponentially fitted finite difference method on Shishkin meshes [32] ($N = 2^{15}, \tau = min\{\frac{1}{4}, -2\sqrt{\varepsilon}ln(\varepsilon)\}$). As shown in **Figure 11**, both reference methods exhibit excellent resolution of the boundary layers, confirming their reliability for singularly perturbed problems. These established schemes therefore serve as robust benchmarks against which the proposed ERSM-sinh method (with $N = 64$) can be validated. More significantly, ERSM-sinh achieves numerical accuracy comparable to that of the established asymptotic method and the Shishkin-mesh scheme, yet it requires substantially fewer grid points. This demonstrates not only the computational efficiency of the sinh-transform approach, but also its practical advantage as a mesh-free, parameter-adaptive method that does not rely on explicit a priori estimation of boundary-layer width.

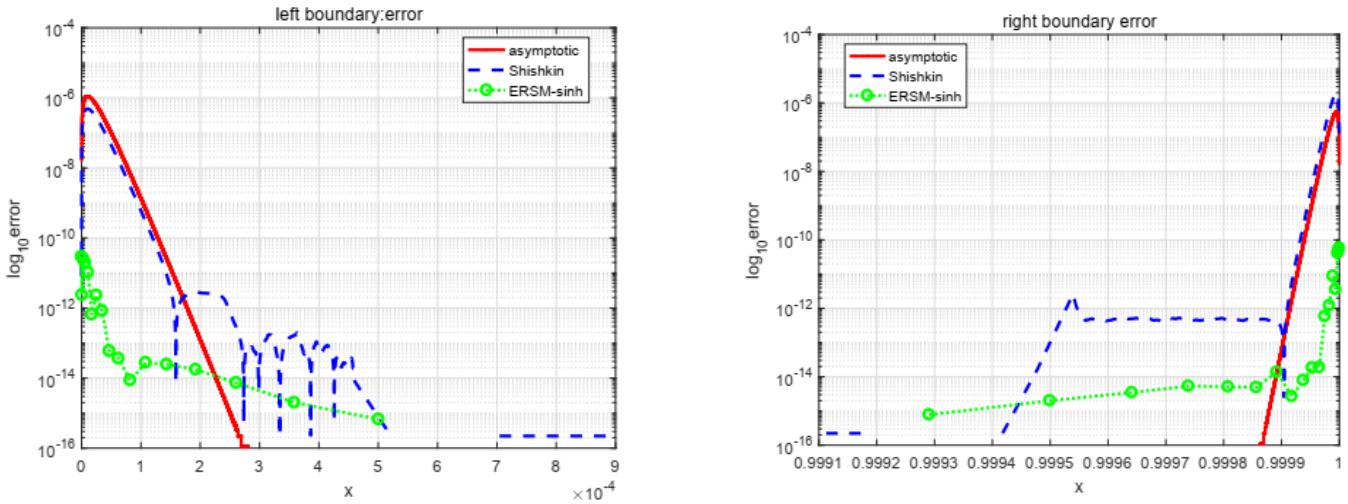

(a) Left. **(b)** Right.

Figure 11. Pointwise errors on boundary layer region in Example 2 ($\varepsilon = 10^{-10}$).

In the absence of an exact analytical solution for certain test problems, we therefore adopt two well-established and mutually-consistent numerical solutions, namely, the classical asymptotic method and the exponentially fitted Shishkin-mesh scheme, as reliable reference benchmarks for subsequent accuracy evaluation.

Example 3. *Consider the variable coefficient singularly perturbed convection-diffusion-reaction problem:*

$$\begin{cases} -\varepsilon u'' + \dfrac{1}{1+x}u' + \dfrac{1}{x+2}u = f(x), \quad 0 < x < 1, \\ u(0) = 1 + 2^{-\frac{1}{\varepsilon}}, \quad u(1) = e + 2. \end{cases}$$

where,

$$f(x) = \left(-\varepsilon + \frac{1}{x+1} + \frac{1}{x+2}\right)e^x + \frac{x+1}{x+2}\left(\frac{x+1}{2}\right)^{\frac{1}{\varepsilon}}.$$

The exact solution of this problem is given as,

$$u(x) = e^x + (x+1)\left(\frac{x+1}{2}\right)^{1/\varepsilon}.$$

As $b(x) = \frac{1}{1+x}$ for $x \in (0,1)$, the problem has a boundary layer at $x = 1$. The corrector function is set as,

$$\theta(x) = e^{\frac{b(1)}{\varepsilon}(x-1)} = e^{\frac{x-1}{2\varepsilon}},$$

and the following equation is satisfied $-\varepsilon\theta''(x) + b(1)\theta(x) = 0$.

The ERSM-sinh solution is obtained by solving the system of Equations (30) and (31). **Table 5** and **Figure 12a** show that for a relatively large perturbation parameter (e.g., $\varepsilon = 10^{-1}$), the standard spectral method (SM) achieves the highest accuracy, whereas the enriched methods (ESM and ERSM-sinh) introduce small errors near the right endpoint. This is consistent with the earlier observation that, in the absence of a sharp boundary layer, the extra collocation points introduced by enrichment are not beneficial and can slightly degrade the approximation.

Figure 12b,c illustrates how the behavior changes as ε decreases: the boundary layer becomes progressively narrower and more localized. Under these conditions, the uniform collocation grids of SM and RSCAT are no longer sufficient to resolve the steep gradient, and their errors increase substantially. In contrast, the enriched methods, through their use of problem-specific corrector functions, are able to capture the rapidly varying layer structure, thereby achieving significantly higher accuracy.

Figure 13 compares the exact solution with the numerical approximations produced by ESM, RSCAT, and ERSM-sinh inside the boundary-layer region. The plot clearly demonstrates the superior performance of ERSM-sinh: its adaptively clustered collocation points, combined with the tailored corrector, enable it to reproduce the fine-scale details of the layer much more faithfully than either ESM or RSCAT. This result underscores the advantage of the proposed method when the perturbation parameter is small and the solution exhibits a sharp boundary layer.

Table 5. Comparison of the maximum relative errors L_∞ for Example 3.

ε	N	SM	RSCAT	ESM	RSC-SSM	ERSM-sinh
10^{-1}	20	2.64×10^{-15}	3.78×10^{-12}	1.03×10^{-14}	5.12×10^{-2}	2.05×10^{-12}
	40	1.86×10^{-14}	1.21×10^{-13}	1.51×10^{-13}	7.15×10^{-2}	2.79×10^{-14}
10^{-2}	20	3.20×10^{-5}	4.36×10^{-7}	3.36×10^{-6}	8.34×10^{-3}	3.66×10^{-8}
	40	2.87×10^{-15}	7.17×10^{-12}	1.33×10^{-13}	1.18×10^{-2}	1.15×10^{-12}
10^{-4}	20	1.17×10^{0}	1.45×10^{-3}	3.58×10^{-16}	6.95×10^{-5}	2.46×10^{-6}
	40	5.01×10^{-1}	2.38×10^{-7}	1.08×10^{-6}	9.87×10^{-5}	1.47×10^{-9}
	60	1.90×10^{-1}	2.99×10^{-10}	1.27×10^{-5}	1.21×10^{-4}	3.22×10^{-11}
10^{-6}	20	1.76×10^{0}	1.06×10^{-1}	1.32×10^{-15}	7.50×10^{-7}	2.04×10^{-9}
	40	1.83×10^{0}	6.85×10^{-7}	1.51×10^{-15}	8.25×10^{-6}	5.84×10^{-10}
	60	1.85×10^{0}	1.15×10^{-7}	8.47×10^{-15}	1.03×10^{-6}	9.56×10^{-10}

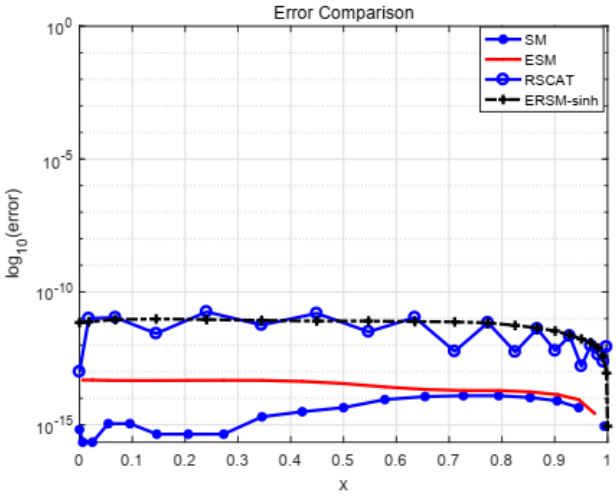

(a) $\varepsilon = 10^{-1}, N = 20$*.

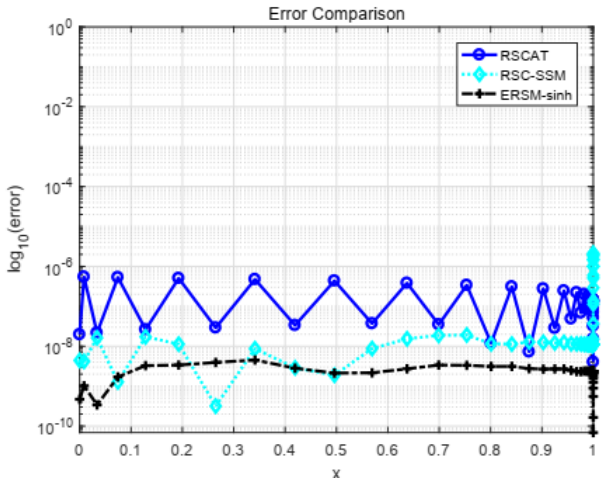

(b) $\varepsilon = 10^{-6}, N = 60$.

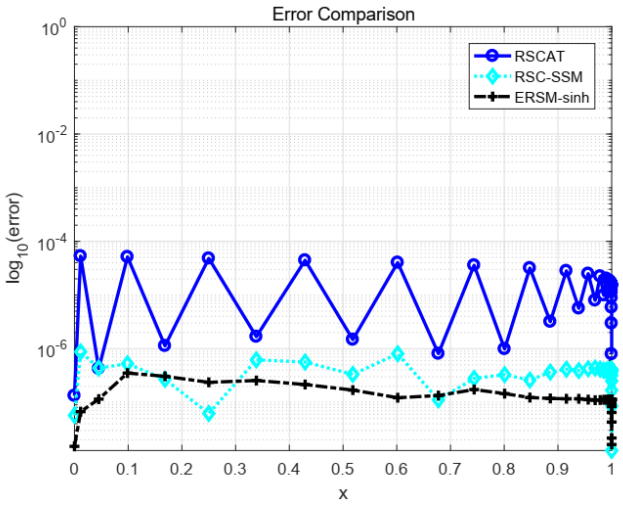

(c) $\varepsilon = 10^{-8}, N = 60$.

Figure 12. The pointwise errors for the different methods.

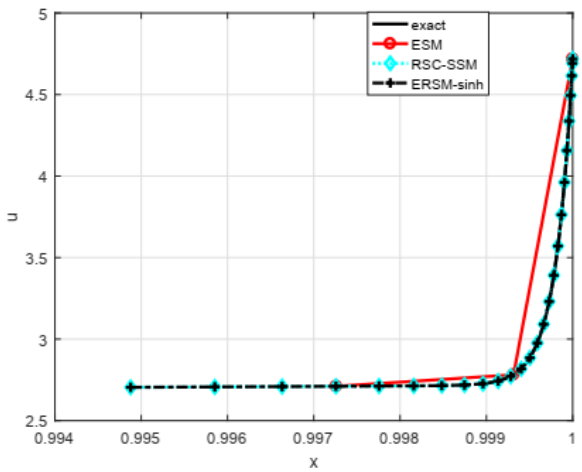

(a) Solution.

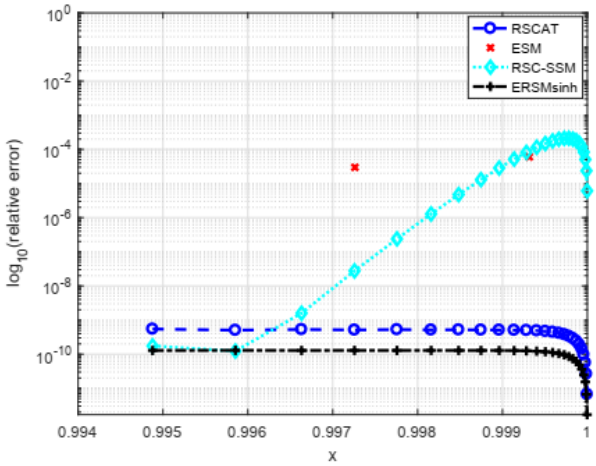

(b) Pointwise error.

Figure 13. Solutions and pointwise errors on the boundary layer region in Example 3 with $\varepsilon = 10^{-4}, N = 60$.

We now evaluate the performance of the ERSM-sinh method for singularly perturbed reaction-diffusion problems whose analytical solutions are unavailable. In

such cases, the double-mesh principle is employed to estimate errors and to compute numerical convergence rates. The maximum absolute error is calculated via the double-mesh formula:

$$E_{\epsilon}^{N} = \max_{0 \le j \le N} \left| u_{j}^{N} - u_{2j}^{2N} \right|, \tag{41}$$

where u_j^N and u_{2j}^{2N} are the jth components of the numerical solutions for N and $2N$, respectively.

Example 4. *Consider the following singularly perturbed reaction-diffusion (i.e., $b(x) = 0$) problem with variable coefficients:*

$$\begin{cases} -\varepsilon u'' + (1+x)^2 u = -1, & 0 < x < 1, \\ u(0) = 0, \quad u(1) = 0. \end{cases}$$

The proposed ERSM-sinh method is applied to solve Example 4. Since an exact solution is unavailable, we estimate the convergence behavior using the double-mesh principle.

Figure 14 illustrates the convergence rate of the ERSM-sinh method for values of a $\varepsilon = 10^{-6}, 10^{-8}$ and 10^{-10}. The method reliably achieves a tolerance of 10^{-8} and exhibits uniform convergence across different values of ε. As the number of mesh points increases, the maximum error decreases consistently, independent of ε. This confirms the ε-uniform convergence of the method, and its robustness for extremely small perturbation parameters is a key characteristic. **Table 6** presents the convergence and computational efficiency of the ERSM-sinh method for different values of ε and N.

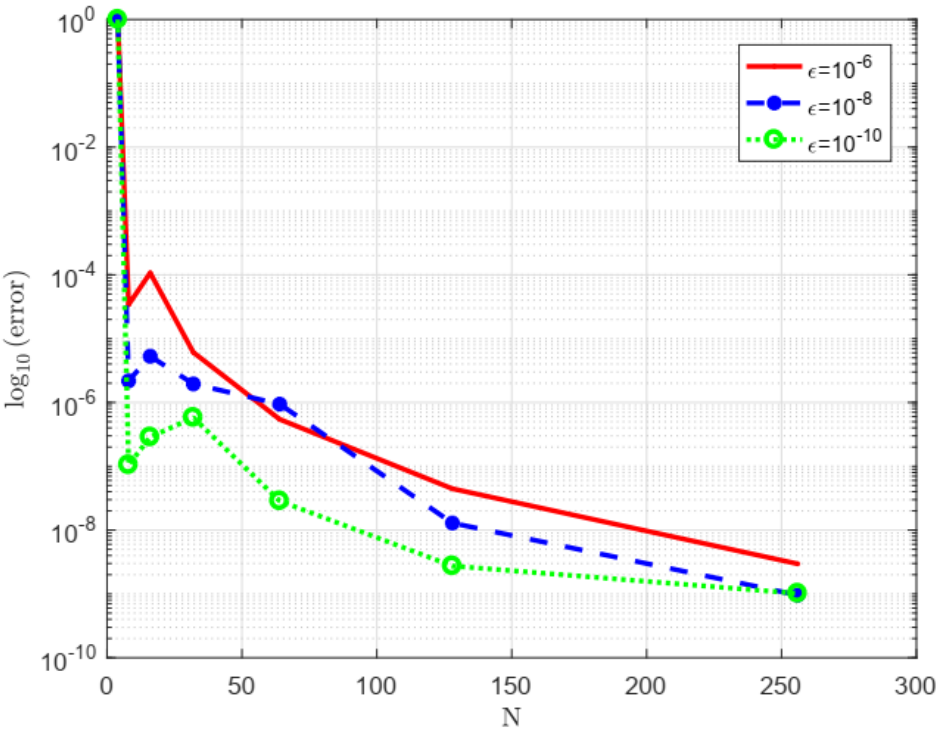

Figure 14. Convergence rates of the ERSM-sinh method for Example 4 with different ε.

Table 6. Maximum relative errors L_∞ and computational time comparison of ERSM-sinh.

N	$\varepsilon = 10^{-6}$		$\varepsilon = 10^{-8}$		$\varepsilon = 10^{-10}$	
	L_∞	$t(s)$	L_∞	$t(s)$	L_∞	$t(s)$
32	6.08×10^{-6}	4.20×10^{-3}	1.95×10^{-6}	4.18×10^{-3}	5.79×10^{-7}	4.24×10^{-3}
64	5.44×10^{-7}	1.22×10^{-2}	9.94×10^{-7}	1.24×10^{-2}	2.86×10^{-8}	1.23×10^{-2}
128	4.45×10^{-8}	1.72×10^{-2}	1.29×10^{-8}	1.81×10^{-2}	2.74×10^{-9}	1.73×10^{-2}
256	2.96×10^{-9}	3.22×10^{-2}	9.59×10^{-10}	3.38×10^{-2}	1.02×10^{-9}	3.26×10^{-2}

Based on the results in **Table 6**, the L_∞ decreases sharply with increasing N for a fixed ε. Moreover, for a given N, the accuracy remains stable or even improves as ε decreases from 10^{-6} to 10^{-10}, demonstrating strong robustness in handling extremely sharp boundary layers. Finally, while computational time grows only modestly with N, accuracy improves by several orders of magnitude, highlighting an excellent trade-off that enables high precision at relatively low computational cost.

Figure 15 displays the numerical solutions of Example 4 computed using the asymptotic expansion method, the exponentially fitted finite difference method on Shishkin meshes, and the proposed ERSM method, along with magnified views of selected regions. The corresponding error distributions are provided in **Figure 16**. A reference solution was constructed by applying cubic spline interpolation to the numerical result from the exponential fitting method on a fine grid with $N = 2^{15}$. For a very small perturbation parameter($\varepsilon = 10^{-10}$), the ERSM-sinh solution achieves high accuracy, closely aligning with the reference solution. This result underscores the method's robustness and effective--ness in resolving singular perturbation problems that challenge conventional approaches.

Figure 16 displays the corresponding error distributions of the asymptotic and ERSM-sinh methods relative to the reference solution. The error of ERSM-sinh is markedly smaller inside the boundary layer, further validating its superior resolution of fine-scale layer structures.

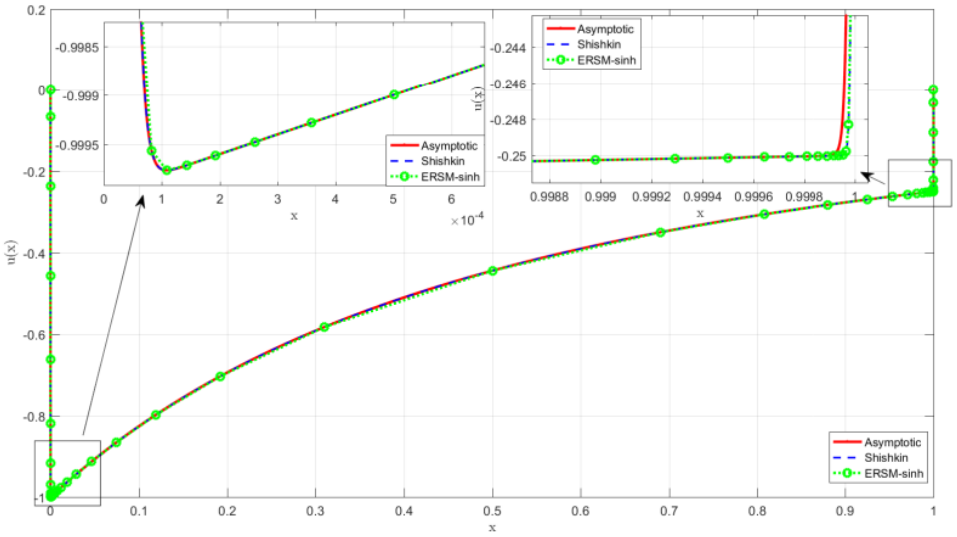

Figure 15. Comparison of numerical solutions by three methods at $\varepsilon = 10^{-10}$ with boundary layer enlargement.

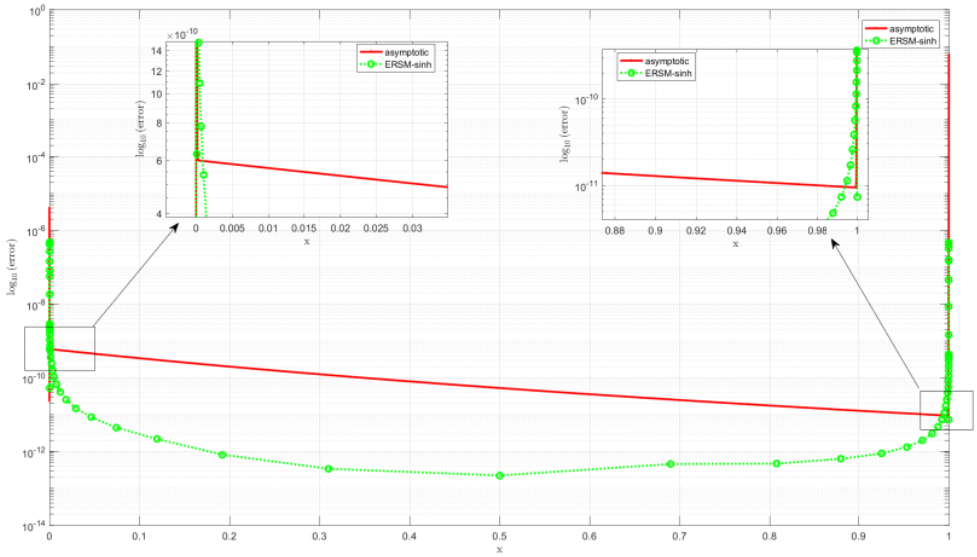

Figure 16. Comparison of error distributions: asymptotic vs. ERSM-sinh methods ($\varepsilon = 10^{-10}$).

The results from Example 4 demonstrate that the proposed ERSM-sinh method is accurate, robust, and computationally efficient. It maintains high precision across a wide range of perturbation parameters, exhibits ε-uniform convergence, and resolves sharp boundary layers effectively, making it a reliable tool for singularly perturbed problems even in the absence of an exact solution.

5. Conclusion and outlook

We have presented and analyzed two high-resolution spectral methods, the Enriched Spectral Method (ESM) and the Enriched Rational Spectral Method with a sinh transformation (ERSM-sinh), for singularly perturbed boundary value problems. The key innovation is the systematic derivation the asymptotic derivation of corrector functions from a variable-coefficient subsidiary problem, which are then used to enrich the spectral approximation space. This enrichment enables the accurate representation of steep gradients inside boundary layers precise capture of solution sharpness within boundary layers. In particular, the ERSM-sinh scheme employs a sinh-transformed collocation grid whose node distribution is guided by asymptotic layer analysis; this strategy proves especially effective as the perturbation parameter decreases and the layers become thinner.

Extensive numerical experiments confirm that both methods, especially ERSM-sinh, achieve near-spectral accuracy and consistently outperform existing approaches for problems with constant or variable coefficients. These results validate the effectiveness of the enrichment framework and the benefit of sinh-based grid adaptation.

5.1. Outlook on multi-dimensional problems

A natural extension of this work is to singularly perturbed problems in two or three dimensions, where boundary layers may appear along edges, corners, or interior interfaces, exhibiting more complex geometries and often anisotropic scaling.

The present methodology, which combines asymptotically derived correctors with a layer-adapted conformal mapping, can be extended to tensor-product domains by using a dimension-wise sinh transform scaled according to the layer width in each coordinate direction. The barycentric rational spectral collocation framework generalizes naturally via tensor-product grids, with corrector functions constructed from the asymptotic description of the associated multi-dimensional layers.

Several significant challenges would emerge in such an extension. First, geometric complexity arises when boundary layers align with curved boundaries or interact in corner regions, necessitating more general coordinate mappings or domain-decomposition strategies. Second, anisotropy in layer widths across different directions requires carefully scaled transforms to maintain resolution. Third, the computational cost escalates rapidly with dimension due to the growth in degrees of freedom; techniques such as sparse grids or low-rank approximations may be needed to preserve efficiency. Addressing these issues will form the focus of future research. The present one-dimensional scheme serves both as a foundational component and a performance benchmark for subsequent multi-dimensional developments.

5.2. Limitations and future work

The current analysis assumes smooth coefficients and source terms. Discontinuities in $b(x)$, $c(x)$, or $f(x)$ can introduce internal layers and compromise global analyticity, which may reduce the convergence rate of spectral methods. A rigorous error analysis for such problems would require a piecewise-analytic framework and careful treatment of interface conditions—an interesting and challenging direction for further research. Extensions to problems with interior discontinuities or strong coefficient variations will be explored in subsequent work.

Funding: This work was supported by Ningxia Basic Science Research Center of Mathematics (No. 2025NXSXZX0202), the Young Talent fostering projects of North Minzu University (No.2023QNPY08), the Natural Science Foundation of Ningxia (No. 2022AAC03287), and the First-Class Disciplines Foundation of Ningxia (No.NXYLXK2017B09).

Institutional review board statement: Not applicable.

Informed consent statement: Not applicable.

Data availability statement: No new data were created.

Conflict of interest: The author declares no conflict of interest.

References

1. Chen Z. Application of singular perturbation in the analysis of laminar premixed flames. Chinese Journal of Theoretical and Applied Mechanics. 2018; 50(6): 1418–1435. doi: 10.6052/0459-1879-18-243 (in Chinese)
2. Zhou LN, Cai TC, Zhao JG, et al. Reinforcement learning-based optimal operational control of complex industrial processes using singular perturbations. Control and Decision. 2025; 40(5): 1581–1589. doi: 10.13195/j.kzyjc.2024.0700 (in Chinese)
3. He Z, Guo Q. Comparative analysis of multiple deep learning models for forecasting monthly ambient PM2.5

concentrations: A case study in Dezhou City, China. Atmosphere. 2024; 15(12): 1432. doi: 10.3390/atmos15121432
4. Roos HG. Robust Numerical Methods for Singularly Perturbed Differential Equations: A Survey Covering 2008–2012. International Scholarly Research Notices. 2012; 2012(1): 379547.
5. Temel Z, Cakir M. A robust numerical method for a singularly perturbed semilinear problem with integral boundary conditions. Contemporary Mathematics. 2024; 5(1): 446–464. doi: 10.37256/cm.5120243020
6. Nefedov NN. Development of methods of asymptotic analysis of transition layers in reaction–diffusion–advection equations: Theory and applications. Computational Mathematics and Mathematical Physics. 2021; 61: 2068–2087. doi: 10.1134/S0965542521120095
7. Alam MJ, Prasad HS, Ranjan R. A new exponentially fitted numerical integration scheme for solving singularly perturbed two point boundary value problems. WSEAS Transactions on Mathematics. 2020; 19: 98–107. doi: 10.37394/23206.2020.19.67
8. Duru H, Demirbaş M. A numerical method for solving singularly perturbed quasilinear boundary value problems on Shishkin mesh. Turkish Journal of Mathematics and Computer Science. 2022; 14(1): 145–154. doi: 10.47000/tjmcs.1010528
9. Raina A, Natesan S. A weak Galerkin finite element method for fourth-order parabolic singularly perturbed problems on layer adapted Shishkin mesh. Applied Numerical Mathematics. 2025; 207: 520–533. doi: 10.1016/j.apnum.2024.09.019
10. Kellogg RB, Xenophontos C. An enriched subspace finite element method for convection-diffusion problems. International Journal of Numerical Analysis and Modeling. 2009; 7(3): 425–442.
11. Han H, Huang Z, Kellogg RB. A tailored finite point method for a singular perturbation problem on an unbounded domain. Journal of Scientific Computing. 2008; 36(2): 243–261. doi: 10.1007/s10915-008-9187-7
12. Wang Y, Cao J, Fu J. Tailored finite point method for time fractional convection dominated diffusion problems with boundary layers. Mathematical Methods in the Applied Sciences. 2020; 47(13): 11044–11061. doi: 10.1002/mma.6772
13. Kong W, Huang Z. A new L1-TFPM scheme for the singularly perturbed subdiffusion equations. CSIAM Transactions on Applied Mathematics. 2025; 6(1): 1–30. doi: 10.4208/csiam-am.SO-2023-0024
14. Jayalakshmi GJ, Tamilselvan A. Second order difference scheme for singularly perturbed boundary turning point problems. Journal of Mathematical Modeling. 2021; 9(2): 201–215.
15. Kellogg RB, Linss T, Stynes M. A finite difference method on layer-adapted meshes for an elliptic reaction-diffusion system in two dimensions. Mathematics of Computation. 2008; 77(264): 2085–2096. doi: 10.1090/S0025-5718-08-02125-X
16. Kabeto MJ, Duressa GF. Accelerated nonstandard finite difference method for singularly perturbed Burger–Huxley equations. BMC Research Notes. 2021; 14(1): 446. doi: 10.1186/s13104-021-05858-4
17. Prince PA, Govindarao L, Elango S. Non-standard finite difference scheme for system of singularly perturbed Fredholm integro-differential equations. Journal of Mathematical Modeling. 2025; 13(4): 501–520.
18. Zhao Q, Wang R, Wang Z, et al. Barycentric rational collocation method for Burgers' equation. Journal of Mathematics. 2022; 2022(1): 2177998. doi: 10.1155/2022/2177998
19. Chen S, Wang Y. A rational spectral collocation method for third-order singularly perturbed problems. Journal of Computational and Applied Mathematics. 2016; 307: 93–105. doi: 10.1016/j.cam.2016.03.009
20. Li J, Su XN, Qu JZ. Linear barycentric rational collocation method for solving telegraph equation. Mathematical Methods in the Applied Sciences. 2021; 44(14): 11720–11737. doi: 10.1002/mma.7548
21. Yang L, Wu YJ. Rational spectral collocation combined with singularity separation method for second-order singular perturbation problems. Journal of Mathematical Sciences. 2023; 270(3): 294–306. doi: 10.1007/s10958-023-06347-8
22. Hwang Y, Jung CY. Enriched spectral method for stiff convection-dominated equations. Journal of Scientific Computing. 2018; 74: 1325–1346. doi: 10.1007/s10915-017-0494-8
23. Shao W, Zheng S. Sinc collocation method and sinh-transform for solving singular perturbed problems with a transition layer. Journal of Xinyang Normal University Natural Science Edition. 2024; 38(1): 92–100. doi: 10.3969/j.issn.2097-583X.2025.01.013 (in Chinese)
24. Gie GM, Hong Y, Jung CY. Semi-analytic PINN methods for singularly perturbed boundary value problems. Applicable Analysis. 2024; 103(14): 2554–2571. doi: 10.1080/00036811.2024.2302405
25. Wang L, Zhang L, He GW. Physics-informed neural networks for solving singularly perturbed boundary-layer problems. Applied Mathematics and Mechanics. 2024; 45(9): 1457–1472.
26. Gol'dberg VN. Stability of a singularly perturbed problem. Differential Equations. 2012; 48(4): 524–537. doi: 10.1134/S0012266112040076
27. de Jager EM, Furu J. The Theory of Singular Perturbations. Elsevier; 1996.

28. Bansal K, Sharma KK, Kaushik A, et al. Numerical analysis of singularly perturbed parabolic reaction diffusion differential difference equations. International Journal of Computer Mathematics. 2024; 101(2): 217–235. doi: 10.1080/00207160.2024.2324455
29. Tee TW, Trefethen LN. A rational spectral collocation method with adaptively transformed Chebyshev grid points. SIAM Journal on Scientific Computing. 2006; 28(5): 1798–1811. doi: 10.1137/050641296
30. Weideman JAC, Trefethen LN. The eigenvalues of second-order spectral differentiation matrices. SIAM Journal on Numerical Analysis. 1988; 25(6): 1279–1298. doi: 10.1137/0725072
31. Armentano MG, Lombardi AL, Penessi C. A finite element analysis in balanced norms for a coupled system of singularly perturbed reaction-diffusion equations. Computational Methods in Applied Mathematics. 2025; 25(2): 235–250. doi: 10.1515/cmam-2023-0219
32. Prathap T, Rao RN. Uniformly convergent finite difference methods for singularly perturbed parabolic partial differential equations with mixed shifts. Applied Mathematics and Computation. 2023; 69: 1679–1704. doi: 10.1007/s12190-022-01802-2